Gradients in cellular metabolism regulate development of tonotopy along the chick cochlea

Thomas S Blacker [2#], James DB O'Sullivan [1#], Val Yianni [1], Mohi Ahmed [1], Zoe F Mann [1*].

[1] Centre for Craniofacial and Regenerative Biology, King's College London

[2] Department of Physics and Astronomy, University College London

[#] Equal primary author contribution

Corresponding author: zoe.mann@kcl.ac.uk

Abstract

In vertebrates with elongated auditory organs, mechanosensory hair cells (HCs) are organised such that complex sounds are broken down into their component frequencies along the basal-to-apical long (tonotopic) axis. To generate the frequency-specific characteristics required at the appropriate positions, nascent HCs must determine their tonotopic properties during development. This relies on complex signalling between the developing HC and its local niche along the axis within the auditory organ. Here we apply NAD(P)H fluorescence lifetime imaging (FLIM) and live imaging of mitochondria to reveal metabolic gradients along the tonotopic axis of the developing chick cochlea. We further show that re-shaping these gradients during development, by inhibiting cytosolic glucose metabolism, alters normal Bmp7 and Chordin like-1 signalling leading to flattening of tonotopic patterning along the axis. Our work supports a causal link between morphogen signalling and metabolic reprogramming in specifying tonotopic morphologies in auditory HCs.

Introduction

Hearing in mammals and lower vertebrates relies on the function of mechanosensory hair cells (HCs) and their associated glial-like supporting cells (SCs). In both mammals and birds, complex sounds are separated into component frequencies by the anatomy of the cochlea, so that different frequencies stimulate HCs located at different positions along the basal-to-apical long axis of the epithelium (tonotopy). This phenomenon underlies our ability to differentiate between the high pitch of a mosquito and the low rumbling of thunder. The specific factors regulating tonotopy remain, largely, unclear. A better understanding of how specific factors regulate tonotopy and, therefore, the formation of frequency-specific HC phenotypes would provide insights regarding both congenital auditory defects and HC regeneration. In particular, high frequency HCs show increased vulnerability to insults, including aging [1], noise damage [2,3] and ototoxicity [4]. Therefore, information regarding the pathways that specify this HC phenotype could identify potential methods to preserve these cells and/or recover high frequency hearing loss.

Metabolism, encompassing the complex network of chemical reactions that sustain life, has emerged as a key regulator of cell fate and differentiation [5]. Instructive roles for glucose metabolism and reprogramming between glycolytic and oxidative pathways has been reported in various systems during development including, for example, delamination and migration in embryonic neural crest [6], hair cells in the zebrafish inner ear [7], specification of trophectoderm fate in the mouse embryo [8] and cell fate decisions along the developing body axis [9-11]. As a complex tissue containing multiple cell types, investigating how metabolism regulates HC formation within the cochlear niche requires experimental approaches capable of interrogating metabolic pathways in live preparations, with single cell resolution. The classic biochemical approaches from which our knowledge of metabolism has formed involve the destructive extraction of metabolites from a sample for subsequent analysis. Probing metabolism in this way, although valuable, means that the spatial organisation of complex

tissues is lost. We have previously exploited the intrinsic fluorescence of reduced nicotinamide adenine dinucleotide (NADH) and its phosphorylated analog NADPH to investigate the metabolic state in HCs and SCs cells of mature cochlear preparations during aging and ototoxicity [12,13]. Both NADH and NADPH serve as reporters of metabolism because they function as redox regulators, transporting reducing equivalents between the enzyme-catalysed reactions of cellular metabolism. Reprogramming of metabolic pathways in tissues causes changes in the time-resolved properties of the NAD(P)H fluorescence signal [14]. Fluorescence lifetime imaging (FLIM) of cellular NAD(P)H therefore provides a non-invasive and label-free method with which to probe metabolism at the single cell level throughout cochlear development [15].

Using previously defined morphological markers of tonotopy as read-outs for unique HC phenotype [16,17] we here investigate a role for metabolism in specifying proximal (high frequency) verses distal (low frequency) HCs. We first identify a gradient in NADPH-linked metabolism along the tonotopic axis of the developing chick cochlea. This gradient is then further confirmed through analysis of metabolic mRNAs and the expression patterns of metabolic effector proteins along the tonotopic axis. We functionally test the role of these gradients by modulating metabolic flux through different branches of glucose metabolism at key stages in HC formation. We find that glucose flux specifically through the pentose phosphate pathway (PPP) instructs tonotopic HC morphologies, by regulating the graded expression of Bmp7 and its antagonist Chordin-like-1, known determinants of tonotopic identity [18]. We also characterise metabolic differences and the timing of this divergence in nascent HCs and SCs. Our findings highlight a novel role for cytosolic glucose metabolism in specifying HC positional identity and provide the first characterisation of unique metabolic states associated with the emergence of HC and SC lineages.

Results

NAD(P)H FLIM reveals differences in the cellular balance of NADPH to NADH along the proximal-to-distal axis of the developing BP.

NAD(P)H FLIM studies in live cells and tissues resolve two fluorescence lifetimes (Figure 1A-D); one with a duration of around 0.4 ns from freely diffusing NAD(P)H (labelled τ_{free}) and the other of 2 ns or more from the pool of NAD(P)H that is bound to enzymes (τ_{bound}) [19,20] (Figure 1C). We have previously shown that the lifetime of enzyme bound (phosphorylated) NADPH is significantly longer than that of bound (unphosphorylated) NADH [14,21]. Changes in τ_{bound} therefore report changes in the cellular NADPH/NADH ratio [12], providing a direct readout of metabolic alterations in living cells. We used this to monitor metabolism along the proximal-to-distal (tonotopic) axis of the BP, both during development and between cell types (Figure 1E-H). At E6 and we observed a significant ($p < 0.05$, Student's *t*-test) difference in τ_{bound} along the tonotopic axis (Figure 1D-I). The proximal-to-distal gradient in τ_{bound} (Figure 1D) was still present at E14, at which time HCs are considered fully differentiated (Figure 1G-J) ($p < 0.05$, Student's *t*-test). In contrast, the gradient was absent at E16. The increased τ_{bound} in the proximal compared to distal BP corresponds to a gradient in metabolic activity along the tonotopic axis between E6 and E14. This suggests that NADPH-producing pathways may regulate developmental refinement of HCs along the tonotopic axis rather than playing a role in their physiological frequency responses, which are apparent from E16 onwards.

FLIM also yields the relative abundance of the bound and free NAD(P)H populations, labelled α_{bound}. Changes in this parameter in response to a range of metabolic perturbations have also been observed[19,22], raising hope of its use as a complementary readout of metabolic state. At present, however, the biochemical relationships linking α_{bound} to metabolic phenotype are less established than for τ_{bound}. Nevertheless, it has previously been suggested that α_{bound} reports shifts in the balance between glycolytic and oxidative ATP production, where a lower α_{bound} reflects a more glycolytic

phenotype [19]. Based on this hypothesis, the changes in α_{bound} we observe here would indicate dynamic shifts between glycolytic and oxidative pathways throughout BP development (Figure 1J).

As HCs and SCs are not easily identified at stages before E9 (Figure 1 D, E), the NAD(P)H FLIM data were initially analysed from the whole epithelium along the proximal to distal axis rather than from specific cell types. However, at E14 and E16 we were able to specifically examine τ_{bound} and α_{bound} in HCs and SCs (Figure 2A, B). We found that both parameters differed significantly between cell types at all positions along the proximal-to-distal axis (Figure 2C, D, E). Additionally, the axial gradient in τ_{bound} (NADPH/NADH ratio) (Figure 2C) in SCs but not HCs is consistent with our results from whole epithelial measurements at E6 and E14 (Figure 1E-J), showing the same metabolic differences as a function of tonotopic position along the cochlea.

Differential expression of mRNAs regulating NADPH production along the tonotopic axis.

Having identified a gradient in the cellular balance of NADPH/NADH along the BP at E6, we sought to investigate the metabolic pathways underlying the differences in τ_{bound} and α_{bound}. By exploiting our previously generated bulk RNA-seq and Affymetrix microarray data sets [18] we measured differential expression of metabolic mRNAs along the BP at E6.5 and E14. In these experiments, BPs had been separated, for bulk RNA-seq and Affymetrix microarray analysis, into proximal, middle, and distal thirds prior to isolation of mRNA [18]. Microarray data were analysed to identify transcripts with expression levels at least two-fold higher in the proximal compared to distal half of the BP. We identified multiple genes with differential expression between proximal and distal regions that are known to regulate NADPH-producing pathways (Figure 3). The largest contributor of cytosolic NADPH is the oxidative branch of the pentose phosphate pathway (PPP) [23]. NADPH can also be generated as a result of mitochondrial tricarboxylic acid (TCA) cycle activity, where levels are maintained through the activity of multiple enzymes [23,24]. Although the specific mRNAs expressed at E6.5 and E14 differ, at both stages metabolic genes showing the highest differential expression between proximal and distal regions were those associated either with diversion of glucose into the PPP or towards aerobic respiration in mitochondria (Figure 3A, B). Together, these expression data reflect differences in NADPH-linked metabolism along the BP. Higher expression of genes regulating NADPH production in the proximal BP (Figure 3) is also consistent with the higher τ_{bound} reported for this region (Figure 1).

Tonotopic expression of metabolic effector proteins.

Modulation of metabolic pathways is driven predominantly through post-translational modifications of metabolic effector proteins [25]. Isocitrate dehydrogenase 3 (IDH3) and Lactate dehydrogenase (LDH) have well-defined roles in regulating the switch between glycolytic and oxidative metabolism during Warburg-like reprogramming [25-28]. They also regulate metabolic flux in the mitochondrial TCA cycle and cytosolic glycolysis respectively (Figure 4A). Therefore, we analysed the expression of IDH3 subunit A and LDH subunit A along the tonotopic axis of the developing BP. There was no difference in IDH3A expression between proximal and distal regions at early stages. However, between E14 and E16, the expression gradient of IDH3A reversed along the tonotopic axis (Figure 4B, C, supplementary Figure 1A). Downregulation of IDH3A has been linked specifically with a switch from oxidative to glycolytic pathways by reducing glucose flux in the mitochondrial TCA cycle [28]. The distal-to-proximal gradient in IDH3a expression at E14 (Figure 4B, D, supplementary Figure 1A) is consistent with a higher cytosolic glucose flux in the low frequency region of the BP. Alongside the higher NADPH/NADH ratio reported for the proximal BP (Figure 1) these findings are consistent with greater PPP activity in the low frequency region and progressively more oxidative metabolic phenotypes towards the distal region. The reversal in the IDH3A gradient at E16 suggesting a shift in metabolic function along the tonotopic axis as the system matures. Studies in other systems have shown that IDH3A regulates

synaptic transmission by controlling vesicle fusion and recycling. Downregulation of IDH3A expression also phenocopies loss of the synaptic Ca^{2+} sensor synaptotagmin1 [29]. The opposing gradient in IDH3A expression at E16 (Figure 4C, D, supplementary Figure 1A) may therefore coincide with the functional refinement of hair cell synapses along the BP at this time. No difference in LDHA expression was seen between proximal and distal regions at any developmental stage. Instead, LDHA expression switched from SCs to HCs between E7 and E10 and was restricted to SCs again between E10 and E14 (supplementary Figure 2). The mechanisms regulating these cell-specific changes in LDHA expression are not known. The timing of these switches does however overlap with important stages in HC development. It will therefore be of interest to investigate potential crosstalk between LDHA-linked metabolism and the developmental pathways that instruct HC and SC specification.

A gradient in glucose uptake is established along the tonotopic axis during BP development.

To further characterise differences in glucose metabolism along the tonotopic axis, we used the fluorescent D-glucose derivative 2-[N-(7-nitrobenz-2-oxa-1,3-diazol-4-yl)-amino]-2-deoxy-D-glucose (2-NBDG) [30] and the potentiometric fluorescent dye tetramethyl-rhodamine-methyl-ester (TMRM). The cellular fluorescence after incubation with 2-NBDG for 2 hours was used as an indicator of glucose uptake. TMRM was used to report mitochondrial membrane potential ($\Delta\Psi_{mt}$), itself a read-out of glycolytically-derived pyruvate oxidation in the mitochondrial tricarboxylic acid (TCA) cycle. Explants were dual-loaded with TMRM and 2-NBDG and fluorescence from both dyes was analysed from single cells in live BP explants between E7 and E16 (Figure 4E-J, supplementary Figure 1B, C). We observed no tonotopic difference in glucose uptake during early development or between HC and SC subtypes. A significant gradient in glucose uptake was evident however along the proximal-to-distal axis at E14 (Figure 4F). There was no significant difference in $\Delta\Psi_{mt}$ between proximal and distal end at any developmental stage, indicating uniform mitochondrial activity along the BP. Despite no differences along the tonotopic axis, $\Delta\Psi_{mt}$ did change significantly ($p < 0.05$ Student's *t*-test) with developmental age (Figure 4H-J, supplementary Figure 1C) reflecting a reprogramming of mitochondrial metabolism during HC formation at a stage when cells are becoming post mitotic [31] . The higher $\Delta\Psi_{mt}$ observed in HCs compared to SCs from E9 may reflect a unique metabolic state that develops in association with commitment to different cell lineages (Figure 4J). These findings also confirm that the gradient in NADPH/NADH (Figure 1D-I) along the BP originates specifically from tonotopic differences in cytosolic and not mitochondrial metabolism.

Cytosolic glucose metabolism is necessary for tonotopic patterning in the chick cochlea.

Having identified differential NADPH-linked glucose metabolism along the proximal-to-distal axis, we next investigated a functional role for this gradient in the establishment of tonotopy. Using 2-deoxy-d-glucose (2-DOG), to inhibit hexokinase (HK) activity, we blocked glycolysis during development [32]. BP explants were established at E6.5 and maintained for 7 days *in vitro* in control medium or that containing 2mM 2-DOG with 5mM sodium pyruvate (NaP), ensuring adequate substrate supply to the TCA cycle. In a normal BP, hair cells are larger in the proximal than the distal region. This gradient is recapitulated in BP explant cultures [18]. In these experiments, HC luminal surface area, a morphometric that is tonotopically driven, was used as a read-out of HC size along the BP. The luminal surface area, measured using Phalloidin staining and HC density, estimated with DAPI, provided read-outs of HC phenotypes at different positions along the tonotopic axis (Figure 5 B, C). In control cultures, HCs developed with the normal tonotopic gradient in morphologies (luminal surface area and density) (Figure 5A, C). In contrast, when glycolysis was blocked between E6.5 and E13.5 equivalent, tonotopic patterning was not just abolished, HC phenotypes appeared flattened and uniformly more distal-like along the BP. To further confirm a role for glycolysis in establishing positional identity, we employed a second method to modulate glucose metabolism. Studies in other systems have shown that raising

186 cytosolic levels of the metabolite s-adenosyl methionine (SAM) blocks glycolysis independently of HK
187 activity [33]. As seen in treatments with 2-DOG, tonotopic patterning was flattened in explants cultured
188 with medium containing 50 μM SAM (supplementary Figure 3).
189
190 A distal-to-proximal gradient of Bmp7 activity is known to establish tonotopy in the BP between E6
191 and E8 [18]. To determine whether glucose metabolism acts during this same developmental window,
192 we treated explants with 2-DOG for defined periods during HC formation. BPs were established at E6.5
193 and treated with 2-DOG for either 24 or 48 hours followed by wash out with control medium. The
194 tonotopic gradient in HC size developed normally in BPs treated with 2-DOG for 24 hours followed by
195 wash-out but was absent in those treated for 48 hours (Figure 5C). These results suggest that glucose
196 metabolism acts during the same developmental time window as Bmp7, establishing the tonotopic
197 gradient in HC size between E6 and E8.
198
199 **Glycolysis, the PPP and pyruvate mediated OXPHOS have distinct roles in HC development.**
200 Glucose metabolism encompasses aerobic glycolysis and the PPP in the cytosol and the TCA cycle in
201 mitochondria, all of which are affected by treatment with 2-DOG. Recent studies in other systems
202 have linked both the PPP and TCA cycle with cell fate decisions during development and differentiation
203 [8,34]. We therefore sought to further dissect the glycolytic signalling network during specification of
204 tonotopy in the developing BP. To investigate a role for PPP-linked glucose metabolism, BP explants
205 were established as described, and treated with 50 μM 6 Aminonicotinamide (6-AN) between E6.5
206 and E13.5 equivalent. Treatment with 6-AN inhibits the rate-limiting PPP enzyme glucose-6-phosphate
207 dehydrogenase (G6PD) (Figure 6C). By comparison with control cultures, inhibition of PPP metabolism
208 caused a significant decrease in hair cell size within 2500 μm^2 areas measured in the proximal BP
209 (Figure 6). To determine whether this effect was specific to glucose flux through the PPP we also
210 blocked phosphofrucktokinase (PFK), a rate limiting enzyme further down in the glycolytic pathway,
211 using 1μM YZ9 (supplementary Figure 4). Blocking PFK activity inhibits the glycolytic cascade involved
212 in pyruvate production but does not change the activity of G6PD in the PPP [8]. Although we observed
213 a reduction in HC size in both BP regions, inhibition of PFK between E6.5 and E13.5 did not alter the
214 intrinsic tonotopic patterning in HCs along the axis of the epithelium ($p = 0.01$ Student's *t*-test proximal
215 verses distal HC size) (supplementary Figure 4). These findings suggest that tonotopic patterning and
216 specification of HC positional identity are regulated by metabolic glucose flux occurring upstream of
217 PFK.

218 Opposing gradients of glucose metabolism and mitochondrial OXPHOS have been described in
219 developing chick embryos, where they regulate elongation of the body axis and specification of cell
220 fates [9]. To investigate a role for the mitochondrial TCA cycle and thus OXPHOS along the tonotopic
221 axis, we blocked the mitochondrial pyruvate carrier using UK5099 (supplementary Figure 5B). [35]
222 Preventing pyruvate uptake into mitochondria inhibits the TCA cycle and, as a result, impairs OXPHOS
223 (supplementary Figure 5B). HCs in explants treated with UK5099 between E6.5 and E13.5 did not
224 develop with normal gradients in HC size along the BP and had either immature stereocilial bundles
225 or lacked them completely in both proximal and distal regions (supplementary Figure 5A, C, red
226 arrows). To determine whether this effect was due to an overall arrest in HC development, explants
227 were established at E8.5, by which time positional identity is specified but bundles are not yet
228 developed and maintained for 7 days *in vitro* to the equivalent of E15.5. Compared to control explants,
229 those treated with UK5099 displayed no tonotopic gradient in cell size and HCs at all positions along
230 the BP showed immature bundle morphologies (supplementary Figure 5C). Together, these findings
231 suggest that mitochondrial TCA cycle activity and OXPHOS are necessary for the overall progression

232 of HC maturation. The role of these pathways in establishing tonotopy is at present unclear and
233 requires further investigation.

234 **Glucose metabolism regulates tonotopic expression of Bmp7 and Chdl-1**

235 In many developing systems, gradients of one or more morphogen act to regulate cell fate, growth
236 and patterning along a given axis [36,37]. In the chick cochlea, reciprocal gradients of Bmp7 and its
237 antagonist Chdl-1 play key roles in determining positional identity. As disruption of both the normal
238 gradient in Bmp7 activity [18] and glucose metabolism induce similar effects on tonotopic patterning
239 (Figure 7A-C), we sought to investigate potential crosstalk between metabolism and known
240 developmental signalling pathways that set up tonotopy. We investigated the regulatory effects of
241 glucose metabolism on the expression gradients of Bmp7 and Chdl-1 along the developing BP. Explants
242 were established at E6.5 and maintained for 72 hours *in vitro* (equivalent of E9.5) in control medium
243 or that containing 2mM 2-DOG + 5mM sodium pyruvate. Disrupting glucose metabolism along the BP
244 altered the normal expression gradients in both Bmp7 and Chdl-1 (Figure 7E). Specifically, following
245 treatment with 2-DOG, the Bmp7 expression increased into the proximal BP region and expression of
246 Chdl-1 decreased along the entire length of the organ. Equalised Bmp7 expression following treatment
247 with 2-DOG caused expansion of HC phenotypes that more closely resembled distal differentiation
248 into the proximal BP. Taken together, our findings indicate a causal link between glycolysis and Bmp7
249 signalling in specifying HC identity along the tonotopic axis.
250

251 **Changes in glucose metabolism do not alter proliferation in the BP**

252 Changes in glucose metabolism have been linked with reduced cellular proliferation in other systems
253 [38]. To determine whether the change in HC morphology observed in 2-DOG treated explants was a
254 result of altered proliferation, the mitotic tracer EdU was added to cultures with 2-DOG for 72 hours.
255 We observed no differences in proliferation in proximal or distal regions following treatment with 2-
256 DOG + 5mM NaP (supplementary Figure 6).
257

258 **A role for NADPH-linked metabolism in the developing mouse cochlea**

259 Unlike in the avian auditory system, HCs in the mammalian cochlea cannot spontaneously regenerate
260 after damage [39]. Although we can generate new HCs using organoid models that recapitulate aspects
261 of early inner development, these cells are not functionally viable long-term and do not display all
262 features of mature HCs [40]. Identifying novel factors and signalling pathways that regulate the
263 specification and formation of HCs and SCs in the mammalian auditory system is therefore of
264 significant interest. Metabolism has not been explored in developing HCs and SCs of the mammalian
265 cochlea. We do know, however, that in the adult cochlea HCs and SCs have distinct metabolic states
266 linked to their function [12]. We therefore characterised the metabolic states of HCs and SCs in the
267 mammalian cochlea between E14 and P0, the developmental window for cell fate specification and
268 functional refinement. As observed in the chick cochlea, there was no difference in the NAD(P)H FLIM
269 signal between HCs and SCs at early developmental stages. At later time points however, there was a
270 significant ($p < 0.05$, Student's t-test) increase in τ_{bound} and α_{bound} between E14 and E16 indicating a
271 metabolic shift (Supplementary Figure 7A-F). The divergence in metabolic state between HCs and SCs
272 during development (supplementary Figure 7D-F) suggests a possible link between metabolic
273 reprogramming and the progression along distinct cell lineages. Similar metabolic reprogramming has
274 been described in differentiating cell types of other complex tissues [5,41].

275 To investigate the biochemistry underlying metabolic differences between HC and SC sub-types, we
276 interrogated existing single cell datasets derived across 3 developmental time points from the mouse
277 cochlea [42]. HCs were identified using expression of *Pou4f3* and lack of *Sox2* [42,43]. Conversely, SCs were
278 identified using expression of *Sox2* [42,44]. We then performed a comparative analysis using the Seurat
279 (v4) package, in R [45,46]. As discussed, an increased τ_{bound} reflects a higher NADPH/NADH ratio,
280 regulated mainly by the PPP activity in the cytosol. We therefore investigated expression of genes

encoding enzymes that regulate PPP metabolism. We found that PPP pathway regulatory enzymes are more highly expressed in SCs compared to HCs at all developmental time points (supplementary Figure 7G). We observed developmental changes in the expression of regulatory enzymes of NADPH metabolism. Increased expression in cytosolic *Nadk*, (generates $NADP^+$ from NAD), in HCs between E14 and E16 (supplementary Figure 7G) likely corresponds to the higher anabolic activity associated with differentiation along the cochlea at this time and thus the greater requirement for PPP-derived NADPH [47]. Additionally at the same time points, we detected a pronounced upregulation in *Pgls,* a major regulator of the PPP and of ribose-5-phosphate production [48]. Heightened availability of this enzyme would provide the necessary biosynthetic precursors for nucleic acid synthesis during cell differentiation [48]. We also investigated differences in the expression of genes encoding regulators of mitochondrial NADPH production (supplementary Figure 7H). We observed that expression of mitochondrial NADPH-producing enzymes is similar between E14 and E16 in both HCs and SCs but becomes restricted to HCs by P1. This likely reflects progressive commitment along the HC lineage, which we know is associated with enhanced mitochondrial activity [42].

Discussion

To successfully address hearing loss and balance defects, we must be able to generate new, functionally viable HCs following damage, aging or ototoxic insult. As certain types of HC are more vulnerable to insult than others, it is essential we understand the specific factors that specify different HC subtypes such as high and low frequency cells. Generating new HCs that recapitulate features of those in a healthy cochlea requires a detailed knowledge their formation. Additionally, we must resolve how they navigate the path of maturation and survival within their surrounding niche along the cochlea. Previous studies have focused largely on understanding the role of transcription factors in HC formation and how manipulation of these in the adult inner ear can be exploited to promote regeneration [43,49-52]. Taking a novel approach, we here explored the coordinated regulation of complex signalling between developmental pathways and metabolism in differentiating HCs and SCs of the inner ear.

Using FLIM imaging of cellular NAD(P)H, we observed a proximal-to-distal gradient in glucose metabolism in the developing BP resulting primarily from tonotopic differences in PPP activity. Analysis of bulk RNA-seq data also identified differentially expressed mRNAs encoding enzymes that divert glucose away from glycolysis and towards the PPP (GOT2 [53], PKM2 [54], PFKFB4 [55,56]) along the tonotopic axis of the developing BP. High levels of NADPH generated through PPP-linked metabolism have been reported in proliferating cells and during differentiation in a number of systems [57]. Graded differences in cell size along the cochlea are important or correct for tonotopy and hearing. Cell size is determined by two opposing processes, growth and division [58] and PPP activity is known to regulate the signalling pathways that coordinate these [59]. The mechanisms linking cell growth, cell cycle progression and cell size regulation are poorly understood in intact tissues such as the cochlea. In the BP, cell cycle exit is initiated in the distal region at embryonic day 5 (E5). Terminal mitosis then progresses in a wave from distal-to-proximal regions and across the neural-to-abneural axis until E9, when the majority of cells are postmitotic [31]. As the critical size for cell cycle progression is determined by environmental factors, one hypothesis is that by differentially regulating growth along the BP and thus timing of cell cycle exit, the gradient in glycolysis could instruct tonotopic differences in HC cell size. Classically, by diverting glucose towards the PPP, nascent cells would be exposed to lower levels of mitochondrially-derived reactive oxygen species (ROS) thus protecting newly synthesised DNA from ROS-induced damage during cell division. Enhanced PPP activity and increased NADPH levels would therefore poise cells for the increased anabolic activity associated with differentiation [57]. At E9, we also see a significant increase in mitochondrial metabolism reported by a more polarised membrane

329 potential and dynamic expression gradients of IDH3A along the BP between E14 and E16.
330 Reprogramming of mitochondrial metabolism is associated with commitment along a given cell
331 lineage [5] suggesting that these changes may correspond to the differentiation state of HCs at this
332 developmental stage.

333

334 Morphogen signalling gradients have well defined roles in directing cell identity along developing axes,
335 where distinct cell subtypes are determined as a function of morphogen concentration at different
336 positions along them [36,60,61]. Glycolysis regulates morphogen signalling in cells of the presomitic
337 mesoderm, where opposing gradients of glycolytic and oxidative metabolism drive elongation of the
338 body axis. Here, glycolysis acts to generate a gradient in intracellular pH (pHi), which modulates the
339 activity of FGF and Wnt signalling pathways along the developing body axis [9-11]. We show a gradient in
340 glucose metabolism along the proximal-to-distal axis of the developing BP that regulates the
341 morphological properties associated with tonotopic identity in HCs. Disruption of this gradient mimics
342 the effects of altered Shh/Bmp/Chordin signalling [18,62], inducing distal-like HC phenotypes in the
343 proximal BP region. Our findings indicate a causal link between developmental and metabolic
344 pathways along the cochlea during HC formation. We know that Sonic Hedgehog (Shh) signalling
345 positively regulates Bmp7 expression in the developing BP and regional identity in the developing
346 mouse cochlea [62]. The mechanisms underlying tonotopy in mammals differ from those in birds and
347 lower vertebrates and although gradients in Bmp7 and Shh are evident along the mammalian cochlea,
348 the downstream targets are not conserved between species [62]. A role for glycolysis in establishing HC
349 positional identity along the mammalian cochlea has not been explored and further studies are
350 needed to determine potential crosstalk between graded metabolism and developmental pathways
351 during development. In the developing drosophila wing, impaired glycolysis causes an upregulation in
352 Hedgehog (Hh) signalling through stabilising the membrane protein Smoothened at the primary cilia.
353 Disrupted glycolysis does not however alter normal levels or the expression pattern of Shh protein
354 within the tissue [63]. The distalisation of HCs in the proximal BP following 2-DOG treatment, may
355 therefore be a consequence of increased Shh activity, which would lead to increased Bmp7 signalling.
356

357 It will be of interest to investigate a role for glucose metabolism in regulating the Shh-Bmp7-Chdl-1
358 signalling network along the proximal-to-distal axis in the chick cochlea and Shh signalling along the
359 basal-to-apical axis in the mouse. Studies in other systems have also identified a role for Shh in
360 regulating glucose metabolism through modulating activity of glycolytic enzymes, [64] most significantly,
361 members of the bifunctional 6-phosphofructo-2-kinase/fructose-2, 6-bisphosphatase (PFKFB 1-4)
362 family [64-66] . The activity of these enzymes is bi-directional, highly regulated at the post-translational
363 level and cell and/or tissue-specific [56]. We show PFKFB4 expression in a proximal-to-distal gradient
364 along the BP at E6.5. A regulatory signalling network between graded Shh, Bmp7 and PFKFB (1-4)-
365 regulated glycolysis has not been explored in any developing tissue but would provide further insight
366 as to how metabolism might fine tune HC phenotypes along the tonotopic axis. Untangling the precise
367 interactions between components of the Sonic Hedgehog-Bmp7-Retinoic acid and glycolytic signalling
368 networks will further our knowledge of how hair cells are tuned during development. From what we
369 understand about frequency selectivity in vertebrates [67], recapitulation of tonotopy will also require
370 that any gradients and the signalling networks they instruct, scale correctly in different inner ear
371 sensory patches and across species with varying head size and cochlear lengths. It will be important
372 to understand how the molecular mechanisms that link metabolic and developmental pathways
373 during HC scale within different inner ear sensory patches and across species.
374

375 Developmental programming of energy balance within HC and SC lineages is an important
376 physiological process allowing cells arising from a common progenitor population to differentiate with
377 unique metabolic states. Extensive changes in cellular redox state occur during the first postnatal week
378 of functional refinement in cells of the mouse cochlea [12,13]. These changes indicate local metabolic
379 switches during the early phases of HC and SC functional maturation [12]. We report cell-specific
380 differences in metabolic enzyme expression, NAD(P)H FLIM signatures and mitochondrial activity in
381 the cochlear epithelium from as early as E14 in mouse and E9 in chick. These cell-specific differences
382 may reflect the developmental origins of metabolic coupling between HCs and SCs. Such cooperation
383 is observed between neurons and astrocytes in the developing brain[68]. Neurons and astrocytes
384 preferentially use different metabolic pathways under physiological conditions, due in part, to cell
385 specific expression patterns of genes regulating energy metabolism [72]. Metabolic coupling is essential
386 for normal brain function and has also been linked with long-term function and survival of cochlear
387 hair cells [69,70]. Long-term hair cell function is not possible without auxilliary input from supporting cell
388 neigbours. Understanding the developmental programs and specific factors that determine future HC-
389 SC coupling within the cochlear niche is essential if we are to recapitulate such mechanisms and
390 sustain long-term HC viability in regenerative or organoid-type models.

391

392 **Materials and Methods**

393 **Embryo care and procedures**

394 Fertilized White Leghorn chicken (*gallus gallus domesticus*) eggs (Henry Stewart & Co. LTD, UK)) were
395 incubated at 37.5°C in an automatic rocking incubator (Brinsea®) until use at specific developmental
396 stages between E6 and E16. Embryos were removed from their eggs, staged according to Hamburger
397 and Hamilton (1951) and subsequently decapitated. All embryos were terminated prior to hatching at
398 E21. All procedures were performed in accord with United Kingdom legislation outlined in the Animals
399 (Scientific Procedures) Act 1986.

400

401 **Preparation of BP and cochleae explants for live imaging studies**

402 Mouse embryos were collected from timed-pregnant females, and cochlear explants were established
403 at E13 to E16 as previously described [71]. For live imaging, the most apical turn of the cochlear duct was
404 removed prior to culturing. Briefly, auditory bullae were removed and transferred into chilled L-15
405 medium (Life Technologies). The wall of the bulla was opened and the whole cochlea extracted. The
406 stria vascularis and Reissner's membrane were removed. All mice were maintained and handled in
407 accord with United Kingdom legislation outlined in the Animals (Scientific Procedures) Act 1986.
408 Explants were placed onto Millicell cell culture inserts (Millipore ®) and incubated overnight at 37°C.
409 Cochlear explants were maintained in Dulbecco's Modified Eagle medium F-12 (DMEM/F-12) and BP
410 explants in medium 199 Earl's salts (M199) (GIBCO, Invitrogen) both containing 2% fetal bovine serum
411 and 5 mM HEPES buffer (Life Technologies). For live imaging experiments explants were transferred
412 to glass-bottom 50 mm MatTek dishes and held in place using custom-made tissue harps (Scientifica).
413 Cultures were maintained in L-15 medium at room temperature throughout the experiment.

414

415 **Basilar papilla culture**

416 Basilar papillae (BPs) were isolated from embryos incubated for between 6 (E6.0) and 8 E8.0) days and
417 maintained in chilled Leibovitz's L-15 media (GIBCO, Invitrogen). Papillae were dissected as described
418 previously [72] and cultured nerve-side-down on Millicell cell culture inserts (Millipore ®). Cell culture
419 inserts were placed into 35 mm culture dishes containing 1.5 mL of medium 199 Earl's salts (M199)
420 (GIBCO, Invitrogen) supplemented with 5 mM HEPES buffer and 2% fetal bovine serum (FBS). Papillae
421 were maintained in M199 medium plus vehicle (control media) for up to 7 DIV until the equivalent of

embryonic day 13.5 (E13.5). For all treatments, a minimum of four samples were analysed. The following factors were applied to experimental BPs in culture at the specified concentrations: 2-Deoxyglucose (2-DOG) 2mM (SIGMA), Sodium Pyruvate (NaP) 5mM (SIGMA), 6-Aminonicotinamide (6AN) 2μM (SIGMA), *S*-(5'-Adenosyl)-*L*-methionine chloride dihydrochloride (SAM) 50μM (SIGMA), YZ9 1μM (SIGMA). For 2-DOG wash-out experiments, cultures were treated for 24 or 48 hours followed by wash out with control medium for the remainder of the experiment up to 7 days. For paired controls, medium was also changed at 24 and 48 hours in culture. At the conclusion of each experiment (7 days *in vitro*), cultures were fixed in 4% paraformaldehyde (PFA) for 20 minutes at room temperature, washed thoroughly three times with 0.1 M phosphate buffered saline (Invitrogen) and processed for immunohistochemistry.

Fluorescence lifetime imaging

NAD(P)H FLIM was performed on an upright LSM 510 microscope (Carl Zeiss) with a 1.0 NA 40x water-dipping objective using a 650-nm short-pass dichroic and 460±25 nm emission filter. Two-photon excitation was provided by a Chameleon (Coherent) Ti:sapphire laser tuned to 720 nm, with on-sample powers kept below 10 mW. Photon emission events were registered by an external detector (HPM-100, Becker & Hickl) attached to a commercial time-correlated single photon counting electronics module (SPC-830, Becker & Hickl) contained on a PCI board in a desktop computer. Scanning was performed continuously for 2 min with a pixel dwell time of 1.6μs. Cells and position within the epithelium was determined prior to FLIM analysis using the mitochondrially targeted fluorescent dye tetramethylrhodamine methyl ester (TMRM). The dye was added to the recording medium, at a final concentration of 350 nM, 45 min before imaging. TMRM fluorescence was collected using a 610±30 nm emission filter. Excitation was provided at the same wavelength as NAD(P)H to avoid possible chromatic aberration. The 585±15 nm emission spectrum of TMRM ensured its fluorescence did not interfere with acquisition of the NAD(P)H FLIM images.

FLIM data analysis

Following 5 x 5 binning of photon counts at each pixel, fluorescence decay curves of the form [12],

$$I(t) = Z + I_0\left([1-\alpha_{\text{bound}}]e^{-t/\tau_{\text{free}}} + \alpha_{\text{bound}}e^{-t/\tau_{\text{bound}}}\right)$$

were fit to the FLIM images using iterative reconvolution in SPCImage (Becker & Hickl), where Z allows for time-uncorrelated background noise. Matrices of the fit parameters τ_{free}, α_{bound} and τ_{bound} and the total photons counted were at each pixel, were exported and analysed for hair cells and supporting cells, and proximal and distal BP regions, using SPCImage and ImageJ software packages.

2-NBDG and TMRM live imaging

The auditory sensory epithelia were isolated from E7, E9, E14 and E16 chick embryos in chilled L-15 medium. BPs were subsequently incubated in 1mM solution of 2-NBDG (N13195, Thermo Fisher Scientific) in L-15 medium at room temperature for 1 hour. The medium was then replaced with a fresh solution of 1mM 2-NBDG and 350 nm TMRM (T668, Thermo Fisher Scientific) in L-15 and incubated for a further hour at room temperature. Afterwards, epithelia were washed several times with fresh medium containing 350 nM TMRM and were mounted in a 3.5 mm glass bottom MatTek dish. 3D image stacks with an optical thickness of 1μm were captured using a Leica SP5 confocal microscope with an HCX PL APO 63×/1.3 GLYC CORR CS (21 °C) objective.

Immunohistochemistry

Inner ear tissue was collected at various developmental stages, fixed for 20 min to one hour in in 0.1 M phosphate buffered saline (PBS) containing 4% paraformaldehyde (PFA), and processed for whole-mounts immunohistochemistry. The auditory sensory epithelium was then fine dissected and permeabilized in PBS containing 0.3% Triton for 30 min before immunostaining using standard procedures. Samples were stained with primary antibodies for LDHA 1:75 (Genetex GTX101416) and IDH3A 1:75 (ab228596, Abcam) and Calbindin 1:50 (ab82812, Abcam). Antibody staining was visualized using secondary antibodies conjugated to either Alexa 488 or Alexa 546 (Invitrogen). Cultures were incubated with all secondary antibodies for 1 hour at room temperature 1:1000, washed thoroughly in 0.1 M PBS. Samples were then incubated for an additional hour with either Alexa Fluor-conjugated Phalloidin-546 (Invitrogen) to label filamentous actin and DAPI 1:1000 to label cell nuclei. Tissue samples were mounted using either Prolong Gold antifade reagent (Invitrogen). 3D image stacks of mounted samples were captured using a Leica SP5 confocal microscope with an HCX PL APO 63×/1.3 GLYC CORR CS (21 °C) objective.

EdU staining

Control or 2-DOG-treated cultures were incubated for 48 hours in 10 µM 5-ethynyl-2'-deoxyuridine (EdU) from embryonic day 6 (E6) to embryonic day 8 (E8). Cultures were subsequently fixed for 15 minutes in 4% PFA at room temperature and then washed in 0.1M PBS. Explants were then processed for EdU staining following the Click-iT® EdU 488 protocol (Thermo Fischer Scientific).

Image analysis

Analysis of z-stacks from IHC stains as well as 2-NBDG and TMRM live imaging experiments was carried out using the Fiji distribution of imageJ. For each sample, a z-plane 2 µm beneath the surface of the epithelium was chosen for further analysis. For each of these selected z-planes, a 100 µm x 100 µm region of interest (ROI) was chosen containing intact tissue in which all HCs were optimally orientated. Mean fluorescence intensity of the tissue was measured for ROIs at E7, E9 and E10 timepoints. At E14 and E16, HCs were manually segmented. HC labels were dilated by 3 µm, which provided selections which included both hair cells and their surrounding SCs. By subtracting the hair cell segmentation from the dilated label, we were thus able to measure the fluorescence intensity of whole HCs separately from their surrounding support cells in the 2-NBDG and LDHA data. A similar approach was adopted when measuring TMRM and IDH3A fluorescence intensity at E14 and E16. However, we noticed that signal was concentrated around the HC periphery. In order to ensure that the fluorescence intensity best reflected only the mitochondria and was not reduced by the low fluorescence from the centre of each HC, we measured mean fluorescence intensity only up to 2 µm from the cell membrane. Likewise, for TMRM and IDH3A data at E7 and E9, mitochondria were segmented using Fiji's auto-local thresholding (Niblack) prior to intensity measurements, to avoid a biased estimate of fluorescence intensity due to empty space surrounding each mitochondrion.

Analysis of hair cell morphology

Data were analysed offline using image J software. Hair cell luminal surface area and cell size were used as indices for HC morphology along the tonotopic axis. To determine the hair cell density, the luminal surfaces of hair cells and cell size, cultures were labelled with phalloidin and DAPI. Then, the number of hair cells in 50 µm × 50 µm regions of interest (2,500 μm^2 total area) located in the proximal and distal BP regions were determined. Proximal and distal regions were determined based a calculation of the entire length of the BP or explant. In addition, counting ROIs were placed in the mid-region of the BP along the neural to abneural axis to avoid any confounding measurements due to radial differences between tall and short hair cells. For each sample, hair cells were counted in four

separate ROIs for each position along the BP. Luminal surface areas were determined by measuring the circumference of individual hair cells at the level of the cuticular plate.

In situ hybridisation

Inner ear tissue was dissected and fixed in 4% PFA overnight at 4 °C. Tissue was subsequently washed three times for 30 min in 0.1 M PBS and subsequently dehydrated in methanol (25–100%). Tissue was stored at −20 °C until use. Immediately before the *in situ* protocol, tissue was rehydrated using a reverse methanol gradient (100–25%). Complimentary digoxigenin-labelled RNA probes for *Bmp7* were kindly provided by Doris Wu (NIDCD, NIH). *Chd-l1* was synthesised as described previously [18]. All *in situ* hybridization reactions were performed as described previously.

Analysis of single cell RNA-seq data sets

Single cell sequencing data was obtained from the study under accession number GSE137299 [42]. The code to process the data was previously shared by the corresponding authors of the above referenced study (https://github.com/kelleylab/cochlearSEscrnaseq). For the purposes of the current analysis, hair cells were extracted from the above dataset using expression of *Pou4f3* and lack of *Sox2* as a metric. This was done for all investigated time points. To identify supporting cells, we used expression of *Sox2* as a metric. The resulting cells were integrated as described in the results section. Briefly, 2000 variable features were identified per type of cell, per time point, and these were used as anchors for integrating the datasets. Gene expression values were then scaled, normalised, and following linear dimensionality reduction, used for cell clustering to project the cells onto a Uniform Manifold Approximation and Projection for Dimension Reduction (UMAP) plot. Genes of interest were then visualised using DotPlots across the different time points.

Acknowledgements

The authors wish to thank Matthew Kelley, Dan Jagger, Jeremy Green, Michael Duchen and Gyorgy Szabadkai and Jonathan Gale for providing comments and discussion on earlier versions of the manuscript. This project was supported by funds from the BBSRC and King's College London.

Author contributions

ZFM, TSB project design and experimental plan.
ZFM, TSB, JO, MA conducted experiments.
ZFM, JO, VY analysed data.
ZFM, TSB, JO, VY wrote and edited the manuscript.

References

1 Gordon-Salant, S. Hearing loss and aging: new research findings and clinical implications. *J Rehabil Res Dev* **42**, 9-24, doi:10.1682/jrrd.2005.01.0006 (2005).
2 Fettiplace, R. & Nam, J. H. Tonotopy in calcium homeostasis and vulnerability of cochlear hair cells. *Hear Res* **376**, 11-21, doi:10.1016/j.heares.2018.11.002 (2019).
3 Wu, F., Xiong, H. & Sha, S. Noise-induced loss of sensory hair cells is mediated by ROS/AMPKalpha pathway. *Redox Biol* **29**, 101406, doi:10.1016/j.redox.2019.101406 (2020).
4 Forge, A. & Richardson, G. Freeze fracture analysis of apical membranes in cochlear cultures: differences between basal and apical-coil outer hair cells and effects of neomycin. *J Neurocytol* **22**, 854-867, doi:10.1007/BF01186357 (1993).
5 Ito, K. & Ito, K. Metabolism and the Control of Cell Fate Decisions and Stem Cell Renewal. *Annu Rev Cell Dev Biol* **32**, 399-409, doi:10.1146/annurev-cellbio-111315-125134 (2016).

561 6 Bhattacharya, D., Azambuja, A. P. & Simoes-Costa, M. Metabolic Reprogramming Promotes
562 Neural Crest Migration via Yap/Tead Signaling. *Dev Cell* **53**, 199-211 e196,
563 doi:10.1016/j.devcel.2020.03.005 (2020).
564 7 Kantarci, H., Gou, Y. & Riley, B. B. The Warburg Effect and lactate signaling augment Fgf-MAPK
565 to promote sensory-neural development in the otic vesicle. *Elife* **9**, doi:10.7554/eLife.56301
566 (2020).
567 8 Chi, F., Sharpley, M. S., Nagaraj, R., Roy, S. S. & Banerjee, U. Glycolysis-Independent Glucose
568 Metabolism Distinguishes TE from ICM Fate during Mammalian Embryogenesis. *Dev Cell* **53**,
569 9-26 e24, doi:10.1016/j.devcel.2020.02.015 (2020).
570 9 Oginuma, M. *et al.* A Gradient of Glycolytic Activity Coordinates FGF and Wnt Signaling during
571 Elongation of the Body Axis in Amniote Embryos. *Dev Cell* **40**, 342-353 e310,
572 doi:10.1016/j.devcel.2017.02.001 (2017).
573 10 Oginuma, M. *et al.* Intracellular pH controls WNT downstream of glycolysis in amniote
574 embryos. *Nature* **584**, 98-101, doi:10.1038/s41586-020-2428-0 (2020).
575 11 Bulusu, V. *et al.* Spatiotemporal Analysis of a Glycolytic Activity Gradient Linked to Mouse
576 Embryo Mesoderm Development. *Dev Cell* **40**, 331-341 e334,
577 doi:10.1016/j.devcel.2017.01.015 (2017).
578 12 Blacker, T. S. *et al.* Separating NADH and NADPH fluorescence in live cells and tissues using
579 FLIM. *Nat Commun* **5**, 3936, doi:10.1038/ncomms4936 (2014).
580 13 Majumder, P., Blacker, T. S., Nolan, L. S., Duchen, M. R. & Gale, J. E. Multiphoton NAD(P)H
581 FLIM reveals metabolic changes in individual cell types of the intact cochlea upon
582 sensorineural hearing loss. *Sci Rep* **9**, 18907, doi:10.1038/s41598-019-55329-x (2019).
583 14 Blacker, T., Marsh, RJ., Duchen, MR., & Bain, AJ. . Activated barrier crossing dynamics in the
584 non-radiative decay of NADH and NADPH. . *Chem. Phys.* **422**, 184-194 (2013).
585 15 Blacker, T. S. & Duchen, M. R. Investigating mitochondrial redox state using NADH and NADPH
586 autofluorescence. *Free Radic Biol Med* **100**, 53-65, doi:10.1016/j.freeradbiomed.2016.08.010
587 (2016).
588 16 Tilney, L. G., Tilney, M. S. & DeRosier, D. J. Actin filaments, stereocilia, and hair cells: how cells
589 count and measure. *Annu Rev Cell Biol* **8**, 257-274, doi:10.1146/annurev.cb.08.110192.001353
590 (1992).
591 17 Goodyear, R. & Richardson, G. Pattern formation in the basilar papilla: evidence for cell
592 rearrangement. *J Neurosci* **17**, 6289-6301 (1997).
593 18 Mann, Z. F. *et al.* A gradient of Bmp7 specifies the tonotopic axis in the developing inner ear.
594 *Nat Commun* **5**, 3839, doi:10.1038/ncomms4839 (2014).
595 19 Skala, M. C. *et al.* In vivo multiphoton microscopy of NADH and FAD redox states, fluorescence
596 lifetimes, and cellular morphology in precancerous epithelia. *Proc Natl Acad Sci U S A* **104**,
597 19494-19499, doi:10.1073/pnas.0708425104 (2007).
598 20 Yu, Q. & Heikal, A. A. Two-photon autofluorescence dynamics imaging reveals sensitivity of
599 intracellular NADH concentration and conformation to cell physiology at the single-cell level.
600 *J Photochem Photobiol B* **95**, 46-57, doi:10.1016/j.jphotobiol.2008.12.010 (2009).
601 21 Gafni, A. & Brand, L. Fluorescence decay studies of reduced nicotinamide adenine
602 dinucleotide in solution and bound to liver alcohol dehydrogenase. *Biochemistry* **15**, 3165-
603 3171, doi:10.1021/bi00660a001 (1976).
604 22 Sanchez, T., Zhang, M., Needleman, D. & Seli, E. Metabolic imaging via fluorescence lifetime
605 imaging microscopy for egg and embryo assessment. *Fertil Steril* **111**, 212-218,
606 doi:10.1016/j.fertnstert.2018.12.014 (2019).
607 23 Bradshaw, P. C. Cytoplasmic and Mitochondrial NADPH-Coupled Redox Systems in the
608 Regulation of Aging. *Nutrients* **11**, doi:10.3390/nu11030504 (2019).
609 24 Ge, T. *et al.* The Role of the Pentose Phosphate Pathway in Diabetes and Cancer. *Front*
610 *Endocrinol (Lausanne)* **11**, 365, doi:10.3389/fendo.2020.00365 (2020).

611 25 Hitosugi, T. & Chen, J. Post-translational modifications and the Warburg effect. *Oncogene* **33**,
612 4279-4285, doi:10.1038/onc.2013.406 (2014).
613 26 Fritz, P. J. Rabbit muscle lactate dehydrogenase 5; a regulatory enzyme. *Science* **150**, 364-366,
614 doi:10.1126/science.150.3694.364 (1965).
615 27 Liu, J. *et al.* Aberrant FGFR Tyrosine Kinase Signaling Enhances the Warburg Effect by
616 Reprogramming LDH Isoform Expression and Activity in Prostate Cancer. *Cancer Res* **78**, 4459-
617 4470, doi:10.1158/0008-5472.CAN-17-3226 (2018).
618 28 Zhang, D. *et al.* Metabolic reprogramming of cancer-associated fibroblasts by IDH3alpha
619 downregulation. *Cell Rep* **10**, 1335-1348, doi:10.1016/j.celrep.2015.02.006 (2015).
620 29 Ugur, B. *et al.* The Krebs Cycle Enzyme Isocitrate Dehydrogenase 3A Couples Mitochondrial
621 Metabolism to Synaptic Transmission. *Cell Rep* **21**, 3794-3806,
622 doi:10.1016/j.celrep.2017.12.005 (2017).
623 30 Yamada, K., Saito, M., Matsuoka, H. & Inagaki, N. A real-time method of imaging glucose
624 uptake in single, living mammalian cells. *Nat Protoc* **2**, 753-762, doi:10.1038/nprot.2007.76
625 (2007).
626 31 Katayama, A. & Corwin, J. T. Cell production in the chicken cochlea. *J Comp Neurol* **281**, 129-
627 135, doi:10.1002/cne.902810110 (1989).
628 32 Barban, S. & Schulze, H. O. The effects of 2-deoxyglucose on the growth and metabolism of
629 cultured human cells. *J Biol Chem* **236**, 1887-1890 (1961).
630 33 Pascale, R. M., Peitta, G., Simile, M. M. & Feo, F. Alterations of Methionine Metabolism as
631 Potential Targets for the Prevention and Therapy of Hepatocellular Carcinoma. *Medicina*
632 *(Kaunas)* **55**, doi:10.3390/medicina55060296 (2019).
633 34 Arnold, P. K. *et al.* A non-canonical tricarboxylic acid cycle underlies cellular identity. *Nature*
634 **603**, 477-481, doi:10.1038/s41586-022-04475-w (2022).
635 35 Zhong, Y. *et al.* Application of mitochondrial pyruvate carrier blocker UK5099 creates
636 metabolic reprogram and greater stem-like properties in LnCap prostate cancer cells in vitro.
637 *Oncotarget* **6**, 37758-37769, doi:10.18632/oncotarget.5386 (2015).
638 36 Towers, M., Wolpert, L. & Tickle, C. Gradients of signalling in the developing limb. *Curr Opin*
639 *Cell Biol* **24**, 181-187, doi:10.1016/j.ceb.2011.11.005 (2012).
640 37 Averbukh, I., Ben-Zvi, D., Mishra, S. & Barkai, N. Scaling morphogen gradients during tissue
641 growth by a cell division rule. *Development* **141**, 2150-2156, doi:10.1242/dev.107011 (2014).
642 38 Zhao, J. *et al.* Low-dose 2-deoxyglucose and metformin synergically inhibit proliferation of
643 human polycystic kidney cells by modulating glucose metabolism. *Cell Death Discov* **5**, 76,
644 doi:10.1038/s41420-019-0156-8 (2019).
645 39 Franco, B. & Malgrange, B. Concise Review: Regeneration in Mammalian Cochlea Hair Cells:
646 Help from Supporting Cells Transdifferentiation. *Stem Cells* **35**, 551-556,
647 doi:10.1002/stem.2554 (2017).
648 40 Koehler, K. R., Mikosz, A. M., Molosh, A. I., Patel, D. & Hashino, E. Generation of inner ear
649 sensory epithelia from pluripotent stem cells in 3D culture. *Nature* **500**, 217-221,
650 doi:10.1038/nature12298 (2013).
651 41 Cliff, T. S. & Dalton, S. Metabolic switching and cell fate decisions: implications for
652 pluripotency, reprogramming and development. *Curr Opin Genet Dev* **46**, 44-49,
653 doi:10.1016/j.gde.2017.06.008 (2017).
654 42 Kolla, L. *et al.* Characterization of the development of the mouse cochlear epithelium at the
655 single cell level. *Nat Commun* **11**, 2389, doi:10.1038/s41467-020-16113-y (2020).
656 43 Driver, E. C. & Kelley, M. W. Development of the cochlea. *Development* **147**,
657 doi:10.1242/dev.162263 (2020).
658 44 Hume, C. R., Bratt, D. L. & Oesterle, E. C. Expression of LHX3 and SOX2 during mouse inner ear
659 development. *Gene Expr Patterns* **7**, 798-807, doi:10.1016/j.modgep.2007.05.002 (2007).
660 45 Hao, Y. *et al.* Integrated analysis of multimodal single-cell data. *Cell* **184**, 3573-3587 e3529,
661 doi:10.1016/j.cell.2021.04.048 (2021).

46 Butler, A., Hoffman, P., Smibert, P., Papalexi, E. & Satija, R. Integrating single-cell transcriptomic data across different conditions, technologies, and species. *Nat Biotechnol* **36**, 411-420, doi:10.1038/nbt.4096 (2018).
47 Ju, H. Q., Lin, J. F., Tian, T., Xie, D. & Xu, R. H. NADPH homeostasis in cancer: functions, mechanisms and therapeutic implications. *Signal Transduct Target Ther* **5**, 231, doi:10.1038/s41392-020-00326-0 (2020).
48 Pelley, J. W. Elsevier's Integrated Review Biochemistry (Second Edition). 75-79, doi: https://doi.org/10.1016/B978-0-323-07446-9.00009-X (2012).
49 Shu, Y. *et al.* Renewed proliferation in adult mouse cochlea and regeneration of hair cells. *Nat Commun* **10**, 5530, doi:10.1038/s41467-019-13157-7 (2019).
50 Taylor, R. R. *et al.* Regenerating hair cells in vestibular sensory epithelia from humans. *Elife* **7**, doi:10.7554/eLife.34817 (2018).
51 Shibata, S. B. *et al.* Gene therapy for hair cell regeneration: Review and new data. *Hear Res* **394**, 107981, doi:10.1016/j.heares.2020.107981 (2020).
52 Tao, L. *et al.* Enhancer decommissioning imposes an epigenetic barrier to sensory hair cell regeneration. *Dev Cell* **56**, 2471-2485 e2475, doi:10.1016/j.devcel.2021.07.003 (2021).
53 Yang, H. *et al.* SIRT3-dependent GOT2 acetylation status affects the malate-aspartate NADH shuttle activity and pancreatic tumor growth. *EMBO J* **34**, 1110-1125, doi:10.15252/embj.201591041 (2015).
54 Dong, G. *et al.* PKM2 and cancer: The function of PKM2 beyond glycolysis. *Oncol Lett* **11**, 1980-1986, doi:10.3892/ol.2016.4168 (2016).
55 Kotowski, K. *et al.* Role of PFKFB3 and PFKFB4 in Cancer: Genetic Basis, Impact on Disease Development/Progression, and Potential as Therapeutic Targets. *Cancers (Basel)* **13**, doi:10.3390/cancers13040909 (2021).
56 Yi, M. *et al.* 6-Phosphofructo-2-kinase/fructose-2,6-biphosphatase 3 and 4: A pair of valves for fine-tuning of glucose metabolism in human cancer. *Mol Metab* **20**, 1-13, doi:10.1016/j.molmet.2018.11.013 (2019).
57 Vander Heiden, M. G., Cantley, L. C. & Thompson, C. B. Understanding the Warburg effect: the metabolic requirements of cell proliferation. *Science* **324**, 1029-1033, doi:10.1126/science.1160809 (2009).
58 A, R. J. *et al.* Cell-size dependent progression of the cell cycle creates homeostasis and flexibility of plant cell size. *Nat Commun* **8**, 15060, doi:10.1038/ncomms15060 (2017).
59 Kaplon, J., van Dam, L. & Peeper, D. Two-way communication between the metabolic and cell cycle machineries: the molecular basis. *Cell Cycle* **14**, 2022-2032, doi:10.1080/15384101.2015.1044172 (2015).
60 Dessaud, E., McMahon, A. P. & Briscoe, J. Pattern formation in the vertebrate neural tube: a sonic hedgehog morphogen-regulated transcriptional network. *Development* **135**, 2489-2503, doi:10.1242/dev.009324 (2008).
61 Sagner, A. & Briscoe, J. Establishing neuronal diversity in the spinal cord: a time and a place. *Development* **146**, doi:10.1242/dev.182154 (2019).
62 Son, E. J. *et al.* Conserved role of Sonic Hedgehog in tonotopic organization of the avian basilar papilla and mammalian cochlea. *Proc Natl Acad Sci U S A* **112**, 3746-3751, doi:10.1073/pnas.1417856112 (2015).
63 Spannl, S. *et al.* Glycolysis regulates Hedgehog signalling via the plasma membrane potential. *EMBO J* **40**, e107925, doi:10.15252/embj.2021107925 (2021).
64 Teperino, R. *et al.* Hedgehog partial agonism drives Warburg-like metabolism in muscle and brown fat. *Cell* **151**, 414-426, doi:10.1016/j.cell.2012.09.021 (2012).
65 Ge, X. *et al.* Sonic hedgehog stimulates glycolysis and proliferation of breast cancer cells: Modulation of PFKFB3 activation. *Biochem Biophys Res Commun* **464**, 862-868, doi:10.1016/j.bbrc.2015.07.052 (2015).

712 66 Di Magno, L. *et al.* Druggable glycolytic requirement for Hedgehog-dependent neuronal and
713 medulloblastoma growth. *Cell Cycle* **13**, 3404-3413, doi:10.4161/15384101.2014.952973
714 (2014).
715 67 Gleich, O., Dooling, R. J. & Manley, G. A. Audiogram, body mass, and basilar papilla length:
716 correlations in birds and predictions for extinct archosaurs. *Naturwissenschaften* **92**, 595-598,
717 doi:10.1007/s00114-005-0050-5 (2005).
718 68 Belanger, M., Allaman, I. & Magistretti, P. J. Brain energy metabolism: focus on astrocyte-
719 neuron metabolic cooperation. *Cell Metab* **14**, 724-738, doi:10.1016/j.cmet.2011.08.016
720 (2011).
721 69 Majumder, P., Duchen, M. R. & Gale, J. E. Cellular glutathione content in the organ of Corti
722 and its role during ototoxicity. *Front Cell Neurosci* **9**, 143, doi:10.3389/fncel.2015.00143
723 (2015).
724 70 Fetoni, A. R. *et al.* Cx26 partial loss causes accelerated presbycusis by redox imbalance and
725 dysregulation of Nfr2 pathway. *Redox Biol* **19**, 301-317, doi:10.1016/j.redox.2018.08.002
726 (2018).
727 71 Driver, E. C., Sillers, L., Coate, T. M., Rose, M. F. & Kelley, M. W. The Atoh1-lineage gives rise
728 to hair cells and supporting cells within the mammalian cochlea. *Dev Biol* **376**, 86-98,
729 doi:10.1016/j.ydbio.2013.01.005 (2013).
730 72 Jacques, B. E. *et al.* The role of Wnt/beta-catenin signaling in proliferation and regeneration
731 of the developing basilar papilla and lateral line. *Dev Neurobiol* **74**, 438-456,
732 doi:10.1002/dneu.22134 (2014).

733
734

Figure Legends

Figure 1. A proximal-to-distal metabolic gradient in the developing chick cochlea.

(A) Two-photon fluorescence image showing NAD(P)H in a live BP explant.

(B) Fluorescence from NADH and NADPH results from redistribution of electronic charge across the amide group of the reduced nicotinamide ring.

(C) NAD(P)H FLIM resolves two components corresponding to freely diffusing (shorter lifetime, τ_{free}) and enzyme bound (longer lifetime, τ_{bound}). The relative proportion of these components is labelled α_{bound}. Changes in τ_{bound} and α_{bound} imply changes in metabolic state.

(D) Schematic of the chick BP, showing the progressive change in cellular NADPH/NADH along the tonotopic axis.

(E-H) FLIM images of the NAD(P)H fluorescence lifetime signal extracted for τ_{bound} in the proximal and distal BP regions at E6 and E14. The mean lifetime signal is ($\tau_{\mathrm{m}} = (1 - \alpha_{\mathrm{bound}})\tau_{\mathrm{free}} + \alpha_{\mathrm{bound}}\tau_{\mathrm{free}}$). A proximal-to-distal gradient is evident in τ_{bound} but not α_{bound} throughout BP development. White asterisks indicate the HCs. Higher magnification images highlight the differences in mean lifetime between proximal and distal HCs at E14.

(I) Quantification of τ_{bound} during development shows a shift from NADPH to NADH producing pathways. Line graphs highlight differences in τ_{bound} between proximal (black) and distal (grey) BP regions throughout development.

(J) α_{bound}**,** reflecting the cellular balance between free and enzyme-bound NAD(P)H, increases significantly in both proximal (black) and distal (grey) BP regions between E6 and E14 and decreases significantly between E14 and E16. Line graphs show differences in α_{bound} in the proximal (black) and distal (grey) regions.

The difference in mean NAD(P)H lifetime result from a shift in the cellular balance of NADPH/NADH, and thus in utilisation of the metabolic pathways that produce these cofactors, from high to low frequency regions. Scale bars = 50μm. Data are mean ± SEM; E6: n = 6, E9: n= 4, E14: n = 7 and E16: n = 6 biological replicates. ***** $p < 0.05$ Student's *t*-test.

Figure 2. Metabolic differences between hair cells and supporting cells along the tonotopic axis of the developing chick cochlea.

(A) Total NAD(P)H fluorescence in the proximal and distal regions of the BP at E16.

(B) Mean fluorescence lifetime signal for NAD(P)H in the proximal and distal BP. Images are mapped using a pseudo colour time scale representing a duration of 2.2 and 4.2 ns. White boxes show the differences in mean lifetime between hair cells (white asterisk, block arrows) and supporting cells (empty arrows).

(C) At E16, τbound is significantly higher in supporting cells (grey bars) compared to hair cells (black bars), indicating distinct metabolic profiles between cell types. The hair-cell-to-supporting cell difference in τbound is higher in the proximal compared to distal BP region.

(D) The cellular proportion of bound NAD(P)H (αbound) is also significantly higher in supporting (grey bars) compared to hair (black bars) again reflecting the cell-specific differences in metabolic pathway utilisation.

(E) Schematic showing a cross-sectional view of the BP at E16. The hair cells (orange) and supporting cells (blue) are indicated. Colours reflect bound lifetime duration in ns shown in (B). Warm colours indicate short lifetimes and cool colours longer lifetimes.

Data are mean ± SEM. * $p < 0.05$, Student's paired *t*-test, n = 10 biological replicates. Scale bars are 50μm.

Figure 3. Differential expression of mRNAs encoding NADPH and NADH regulatory enzymes in the chick basilar papilla.

(A-B) Bulk RNA-seq data showing differential expression of genes that regulate the cellular NADPH/NADH ratio. Data show the normalised RPKM values in the proximal and distal BP regions at E6.5 (normalised reads per kilobase of transcript per million mapped reads). All genes with a Log_2 >1 are significantly expressed in the distal BP region and all genes with a Log_2 <1 are expressed significantly in the proximal BP region. Statistical significance levels were calculated by one-way ANOVA. For a gene to be considered 'differential', at least one region of the BP (proximal, middle or distal) was required to be ≥0.5 RPKM. A fold change of ≥ 2 was imposed for the comparison between distal and proximal regions. A final requirement was that middle samples had to exhibit RPKM values mid-way between proximal and distal regions to selectively capture transcripts with a gradient between the two ends.

(C) Affymetrix array data showing the differential expression of mRNAs encoding enzymes that regulate NADPH-production. Data was analysed to show fold change in expression of each transcript at the proximal compared to the distal region of the BP at E14. Microarray signals were normalized using the RMA algorithm. The mRNAs expressed at significantly different levels in distal versus proximal BP were selected based on ANOVA analysis by Partek Genomics Suite software (Partek, St. Charles, MO, USA) ***** $p < 0.05$.

ALDH1A3 - Aldehyde Dehydrogenase 1 Family Member A3, GOT2 - Glutamic-Oxaloacetic Transaminase 2, LDHB – Lactate dehydrogenase beta, PFKFB4 - 6-Phosphofructo-2-Kinase/Fructose-2,6-Biphosphatase 4, PKM2 – Pyruvate kinase M2, LDHA – Lactate dehydrogenase alpha, NNT - Nicotinamide Nucleotide Transhydrogenase, IDH3B – Isocitrate dehydrogenase beta, IDH3A - Isocitrate dehydrogenase alpha.

Figure 4. Glucose uptake and mitochondrial metabolism vary with developmental age, cell type and position along the tonotopic axis.

(A) Schematic showing IDH3 activity in the mitochondrial TCA cycle.

(B, C) Developmental expression of the mitochondrial TCA cycle enzyme IDH3A. Images show BP explants at E14 and E16 stained with Phalloidin, as a marker of filamentous Actin and labelled for IDH3 subunit A. Expression of IDH3A was significantly reduced at E14 compared to E7 and E10, both in proximal and distal regions. At E14 a distal-to-proximal gradient in IDH3A expression is established and by E16 this gradient is reversed along the BP.

(D) Quantification of IDH3A expression in proximal (black bars) and distal (grey bars) BP regions throughout development.

(E) 2-NBDG fluorescence in live BP explants shows no difference in glucose uptake along the proximal-to-distal axis or between cell types during development.

(F) Quantification of glucose uptake, as indicated by 2-NBDG fluorescence, in proximal (black bars) and distal (grey bars) BP regions between E7 and E14.

(G) Analysis of 2-NBDG fluorescence in hair cells and supporting cells at E14.

(H) Mitochondrial membrane potential measured using TMRM fluorescence in single z-planes from image stacks in the proximal and distal regions of live BP explants.

(I) Quantification of TMRM fluorescence indicates a significant increase in mitochondrial activity between E7 and E9, followed by significant decrease between E9 and E14.

(J) TMRM fluorescence is significantly higher in hair cells compared to supporting cells in proximal and distal BP regions at E10 and E14.

All data are represented as means ± SEM. For TMRM n = 6 biological replicates for E7, E10, E14. p = 0.04, and 0.002 Student's *t*-test. HCs vs SCs, proximal: n = 6 biological replicates, p = 0.035 and 0.039 for proximal and distal regions respectively, Student's *t*-test. IDH3A: E7 n=3, E10 n=3, E14 n=5 biological replicates. $P < 0.05$ Student's *t*-test. Scale bars = 40 µm.

834 **Figure 5. Blocking glycolysis at key stages of cochlear development induces distal-like phenotypes**
835 **in the proximal BP.**
836 **(A-B)** Maximum z-projections of BP explants showing Phalloidin and DAPI staining in the proximal and
837 distal regions. Explants were maintained from E6.5 for 7 days *in vitro* (equivalent to E13.5) in either
838 control medium or medium supplemented with 2mM 2-DOG + 5 mM Sodium Pyruvate (NaP).
839 Phalloidin staining depicts differences in hair cell morphology between proximal and distal regions
840 and DAPI indicates the gradient in hair cell size.
841 **(C)** Quantification of these differences**.** Hair cell luminal surface area was measured in 2500 μm^2 areas
842 in the proximal (black bars) and distal (grey bars) BP regions for all culture conditions. In controls,
843 mean hair cell luminal surface decreases progressively from the proximal-to-distal region. This
844 gradient is abolished if glycolysis is blocked with 2-DOG between E6.5 and E13.5. 2-DOG caused a
845 significant decrease in hair cell size in the proximal but not distal region. 2-DOG treatments were
846 reduced to 24 or 48 hours to identify the developmental time window during which glycolysis takes
847 effect. Following wash-out of 2-DOG after 24h, explants developed with normal hair cell positional
848 identity and showed a significant decrease in luminal surface area along the proximal-to-distal axis.
849 Explants treated with 2-DOG for 48 hours showed no recovery of positional identity following wash-
850 out indicated by the loss of gradient in hair cell morphology.
851 **(D)** The target of 2-DOG inhibition.
852 Data are mean $\pm$ SEM. ***** $p < 0.05$ Student's paired *t*-test. Controls; n = 4, 2-DOG; n = 5, 24 2-DOG, n =
853 3 and 48h 2-DOG; n = 3 biological replicates. To ensure adequate substrate supply to the TCA cycle, 2-
854 DOG-treated explants were supplemented with NaP. G6P glucose 6-phosphate, F6P – fructose 6-
855 phosphate, F16BP – fructose 1,6-bisphosphate, 2-DOG – 2-deoxyglucose. Scale bars are 20 μm.
856

857 **Figure 6. Glycolytic flux through the pentose phosphate pathway modulates hair cell development**
858 **and positional identity along the tonotopic axis of the BP.**
859 **(A-B)** Maximal z-projections of BP explants cultured from E6.5 for 7 days *in vitro* with control medium
860 or medium containing 2 μM 6-AN. Images show the epithelial surface in proximal and distal BP regions
861 stained with Phalloidin.
862 **(C)**Treatment of explants with 6-AN, a specific blocker of glycolytic flux through the pentose phosphate
863 pathway, caused a significant reduction in proximal compared to distal hair cell size and disrupted the
864 normal tonotopic gradient in Calbindin expression.
865 **(D)** Quantification of hair cell size using measurement of the cuticular plate in defined 2500^2 μm areas
866 in the proximal (black bars) and distal (grey bars) BP regions. Hair cell luminal surface area was
867 quantified using Phalloidin staining. Data are mean $\pm$ SEM. * $p < 0.05$ Student's paired *t*-test. Controls:
868 n = 5, 6-AN: n = 6 biological replicates. Scale bars are 10μm. G6P – glucose 6-phosphate, F6P – fructose
869 6-phosphate, F16BP – fructose 1,6-bisphosphate.
870

871 **Figure 7. A tonotopic gradient in NAD(P)H producing glucose metabolism specifies hair cell**
872 **positional identity along the BP by regulating gradients of Bmp7 and Chordin like-1.**
873 **(A**) Phalloidin staining at the surface of BP explants in the proximal and distal regions. Explants were
874 established at E6.5 and incubated for 7 days *in vitro* in control medium or medium containing 2-DOG
875 + NaP or Bmp7.
876 **(B-C)** Treatment with 2-DOG or Bmp7 induced hair cell morphologies consistent with a more distal
877 phenotype in the proximal BP. Hair cell luminal surface area was determined using Phalloidin staining
878 at the cuticular plate in 2500^2 μm areas at both proximal and distal ends.
879 **(D)** Schematic of the chick BP, showing the graded differences in hair cell size and density along the
880 tonotopic axis. The opposing gradients in Bmp7 activity and the cellular NAD(P)H/NADH ratio are
881 indicated.
882 **(E)** Treatment of explant cultures with 2-DOG + NaP from E6.5 for 7 days *in vitro* disrupts the normal
883 tonotopic expression gradients of Bmp7 and its antagonist Chordin like-1. Images show *in situ*

884 *hybridisation* for *Bmp7* and *Chordin like-1* in BP whole-mounts treated with 2-DOG +NaP from E6.5 for
885 7 days *in vitro*. Note the disruption of both gradients when glycolysis is blocked during development.
886 Controls: n=8, 2-DOG: n=6 Data mean ± SEM. * $p < 0.05$ Student's *t*-test. Scale bars (A) control, DOG
887 are 20 μm and Bmp7 is 50 μm. Scale bars (E) are 10μm.
888
889 **Supplementary Figure legends**
890
891 **Supplementary Figure 1.** Line graphs showing the trends in **(A)** IDH3A expression, **(B)** 2-NBDG and
892 **(C)**TMRM fluorescence and along the proximal-to-distal axis of the developing BP. Data are mean ±
893 SEM, $p < 0.05$, Student's *t*-test. n = 4 for IDH3A; n = 6 for 2-NBDG; n = 6 for TMRM.

894 **Supplementary Figure 2. Changes in the cell-specific expression of the glycolytic regulator LDHA**
895 **during cochlear development.**
896 **(A**) BP explants stained with Phalloidin and labelled for the metabolic enzyme LDHA. Phalloidin marks
897 the hair cells at different stages of cochlear development (E7-E14). At E7, LDHA expression is localised
898 to supporting cells. By E10 expression is restricted to the hair cells.
899 **(B)** No differences in LDHA expression were evident along the proximal-to-distal axis of the BP at any
900 developmental stage. Indicating a reprogramming of glucose metabolism, the expression of LDHA
901 reduced significantly in the proximal (black bars) but not distal (grey bars) region at E14. Data are
902 mean ± SEM. * $p < 0.05$ Student's *t*-test.
903
904 **Supplementary Figure 3. Modulating S-Adenosyl methionine during development abolishes the**
905 **gradient in hair cell morphology along the tonotopic axis of the BP.**
906 **(A-B)** Images are maximal z-projections of proximal and distal regions from BP explants maintained
907 for 7 days *in vitro* in control medium or medium containing 50 μM SAM. Phalloidin staining (A, B top
908 panels) shows the BP surface and hair cell luminal surface areas and DAPI staining (A, B bottom panels)
909 shows the hair cell size and density along the proximal-to-distal axis.
910 **(C)** Treatment of explants with SAM from E6.5 for 7 days *in vitro* abolished the normal gradient in hair
911 luminal surface area along the tonotopic axis. This effect was most pronounced in the proximal
912 compared to distal region. Hair cell luminal surface areas were measured from 2500 μm^2 areas in the
913 proximal (black bars) and distal (grey bars) BP regions of control and SAM-treated explants.
914 **(D)** Schematic showing how increasing SAM levels indirectly modulates glycolytic flux.
915 Data are mean ± SEM. ***** $p < 0.05$ Student's paired *t*-test. Controls: n = 5 and SAM: n = 4 biological
916 replicates. Scale bars are 20 μm. MYC - MYC Proto-Oncogene, BHLH Transcription Factor, SAM - S-
917 Adenosyl methionine, PP2A – protein phosphatase 2, AKT - *Akt* serine/threonine kinase family,
918 LKB1/AMPK – serine threonine kinase pathway in volved in metabolic regulation.
919

920 **Supplementary figure 4. Inhibiting phosphofructokinase has no effect on hair cell positional**
921 **identity in the developing BP.**
922 **(A)** Maximal z-projections showing Phalloidin staining in proximal and distal BP regions of control
923 and YZ9-treated explants.
924 **(B)** Blocking glycolysis at the level of PFK between E6.5 and E13.5 had no effect on hair cell morphology
925 along the tonotopic axis. Hair cell circumference was quantified in 2500 μm^2 areas in proximal (blue
926 bars) and distal (orange bars) regions, showing no difference in size or density after treatment with
927 1μM YZ9.
928 **(C)** Schematic illustrating the inhibitory action of YZ9 in the glycolytic pathway.
929 Data are mean ± SEM. * $p < 0.05$ Student's paired *t*-test. Controls: n = 4, YZ9: n = 3. Scale bars are 20
930 μm. Red circles indicate size hair cell luminal surface area between control and YZ9-treated explants.
931 G6P – glucose 6-phosphate, F6P – fructose 6-phosphate, F1, 6BP – fructose 1,6-bisphosphate.
932

933 **Supplementary Figure 5. Mitochondrial OXPHOS is necessary for the normal developmental**
934 **progression of hair cells but not positional identity.**
935 **(A)** Hair cell morphology at the surface of the BP epithelium in explants stained with Phalloidin.
936 Cultures were established at E6.5 and maintained for 7 days *in vitro* in control medium of that
937 supplemented with the mitochondrial inhibitor UK5099.
938 **(B)** Blocking pyruvate uptake into mitochondria with UK5099 disrupts normal TCA cycle activity and
939 thus mitochondrial OXPHOS.
940 **(C)** Blocking mitochondrial metabolism Between E6.5 and E13 resulted in developmental
941 abnormalities in HCs along the BP and a significant reduction in hair cell size in the proximal region.
942 Stereocilia bundles of hair cells in the proximal BP region (red arrows) appeared immature compared
943 to controls and those at the distal end. To determine whether mitochondrial OXPHOS acts during a
944 specific developmental time window, cultures were treated with 1μM UK5099 for 7 days *in vitro* from
945 E6.5 or for 5 days *in vitro* from E8.5. These times points are both be equivalent developmentally to
946 E13.5. for Proximal hair cells showed no recovery following UK5099 wash-out. Data are mean ± SEM.
947 * $p < 0.05$, Student's *t*-test.
948
949 **Supplementary Figure 6. 2-Deoxyglucose does not alter proliferation in the developing BP.**
950 Images are maximal z-projections of the sensory epithelium in BP explants treated for 24 hours *in vitro*
951 with either control (top) or 2-DOG + sodium pyruvate supplemented (bottom) medium. Cultures are
952 stained with EdU (green) as a marker for proliferation and Hoechst to label cell nuclei (grey). Cultures
953 were established at E7 and treated for 24 hours to *in vitro* capturing the period of active proliferation
954 in the epithelium.
955
956 **Supplementary Figure 7. Hair cells and supporting cells in the mammalian cochlea show**
957 **differential expression of genes regulating cellular NADPH/NADH.**
958 **(A-B)** NAD(P)H fluorescence in live cochlear explants at E14 and E16.
959 **(C-D)** NAD(P)H lifetime images extracted for α_{bound} at E14 and E16. Differences in α_{bound} show
960 switching between glycolytic and oxidative metabolism during cochlear development. Insets highlight
961 differences in α_{bound} and thus metabolism between HCs (black bars) and SCs (grey bars) at E16 but not
962 E14. White arrows indicate the SCs and white circles outline the HCs.
963 **(E)** τ_{bound} increases in both HCs (black bars) and SCs (grey bars) between E14 and E16 and decrease
964 significantly in both cell types between E16 and P0**.** The change in τ_{bound} indicates a shift in the cellular
965 NADPH/NADH balance as a function of development. At E16, τ_{bound} is significantly higher in SCs (grey
966 bars) compared to HCs (black bars) showing metabolic divergence between cell types as a function of
967 development.
968 **(F)** α_{bound}, reflects the proportion of cellular NAD(P)H that is bound to either enzymes or cofactors and
969 the balance between glycolysis and OXPHOS. α_{bound} increases significantly in both hair cells and
970 supporting cells between E14 and E16 but decreases significantly in supporting cells only between E16
971 and P0**.** This indicates a reprogramming of metabolic pathways both developmentally and between
972 cell types. Data are mean ± SEM. * $p = < 0.05$ Student's paired *t*-test. E14: n = 3, E16: n = 5 and P0, n =
973 5 biological replicates. Scale bars are 50 μm.
974 **(G-F)** Dot plot visualisation of genes encoding key enzymes that regulate cellular levels of NAD(P)H
975 across HCs and SCs at different stages of murine cochlea development. Size of dots encodes
976 percentage of cells expressing the named gene, while colour encodes the average expression of that
977 genes across the cells within each group. Genes shown are for NAD(P)H regulation via the pentose
978 phosphate pathway (G) or in the mitochondria (F)**.**
979
980
981

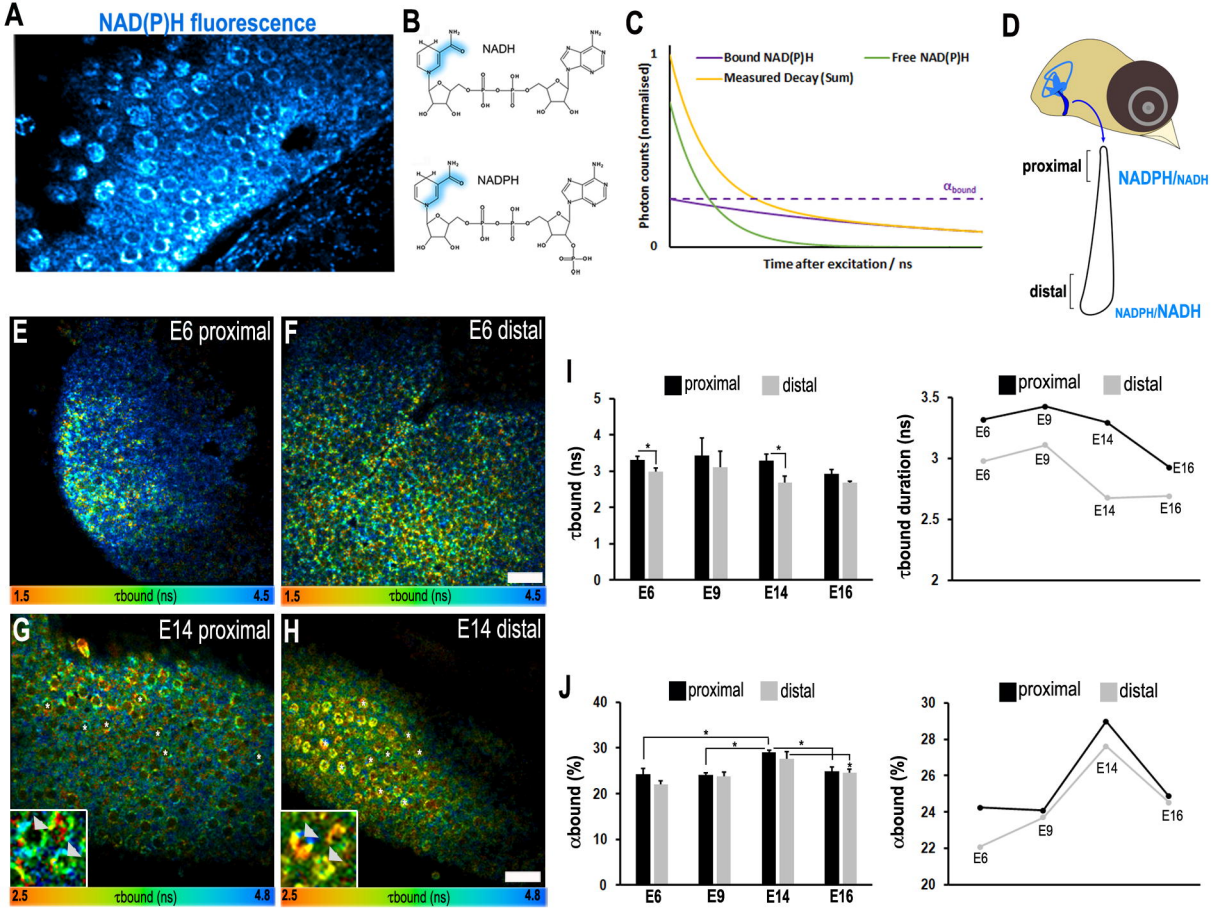
A
NAD(P)H fluorescence
B
NADH
NADPH
C
Bound NAD(P)H
Free NAD(P)H
Measured Decay (Sum)
Photon counts (normalised)
Time after excitation / ns
α_{bound}
D
proximal
NADPH/NADH
distal
NADPH/NADH
E
E6 proximal
F
E6 distal
1.5
τbound (ns)
4.5
G
E14 proximal
H
E14 distal
2.5
τbound (ns)
4.8
I
proximal
distal
τbound (ns)
E6
E9
E14
E16
τbound duration (ns)
J
αbound (%)

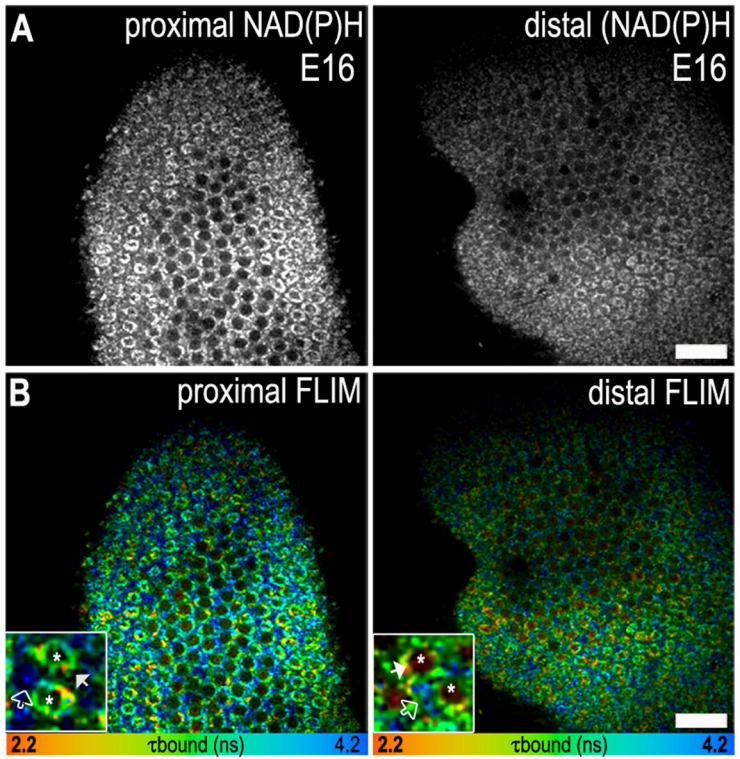
A
proximal NAD(P)H
E16
distal (NAD(P)H
E16
B
proximal FLIM
distal FLIM
2.2
τbound (ns)
4.2
2.2
τbound (ns)
4.2

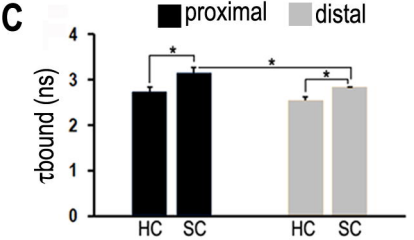
C
proximal
distal
τbound (ns)
0
1
2
3
4
HC
SC
HC
SC

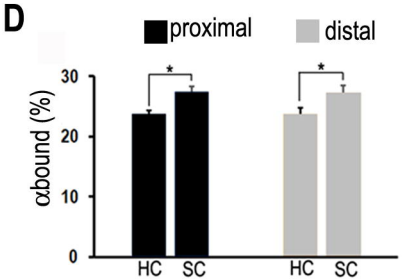
D
proximal
distal
αbound (%)
0
10
20
30
HC
SC
HC
SC

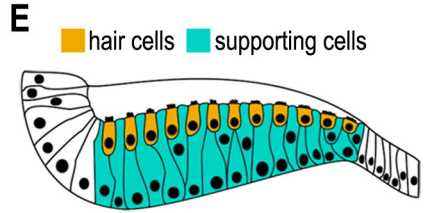
E
hair cells
supporting cells

A

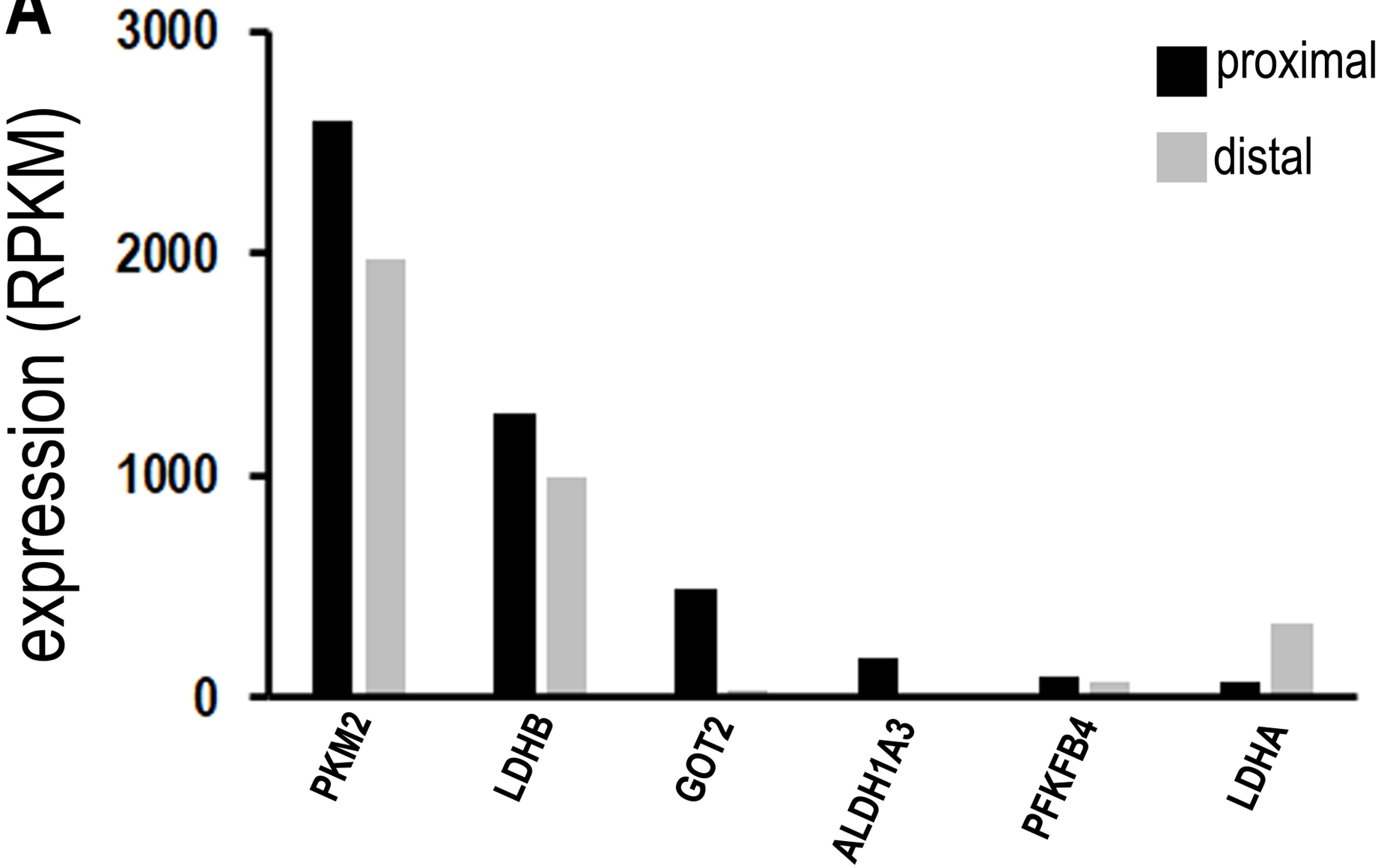

B

E6.5			
Gene	Proximal	Distal	Log_2
ALDH1A3	177.65	9.26	-4.6
GOT2	481.83	29.36	-0.7
LDHB	1277.25	993.42	-0.3
PFKFB4	93.61	70.87	-0.4
PKM2	2591.581	1979.26	-0.3
LDHA	70.16	333.28	2.24

C

E14	
Gene	Fold change
ALDH1A3	19
GOT2	1.6
NNT	1.5
IDH3B	1.4
IDH3A	-1.6

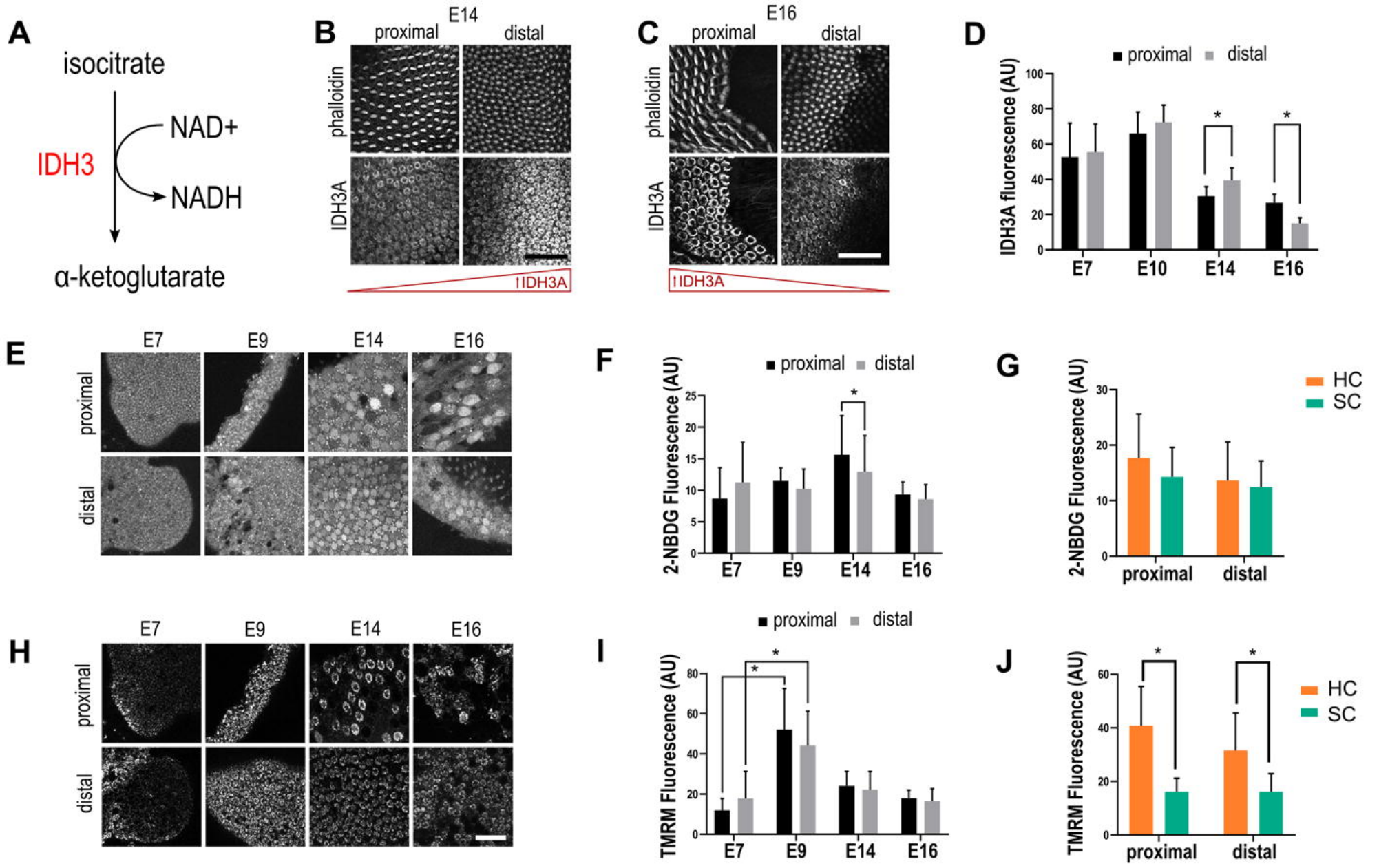
A
isocitrate
NAD+
IDH3
NADH
α-ketoglutarate
B
E14
proximal
distal
phalloidin
IDH3A
↑IDH3A
C
E16
proximal
distal
phalloidin
IDH3A
↑IDH3A
D
proximal
distal
IDH3A fluorescence (AU)
E7
E10
E14
E16
E
E7
E9
E14
E16
proximal
distal
F
proximal
distal
2-NBDG Fluorescence (AU)
E7
E9
E14
E16
G
HC
SC
2-NBDG Fluorescence (AU)
proximal
distal
H
E7
E9
E14
E16
proximal
distal
I
proximal
distal
TMRM Fluorescence (AU)
E7
E9
E14
E16
J
HC
SC
TMRM Fluorescence (AU)
proximal
distal

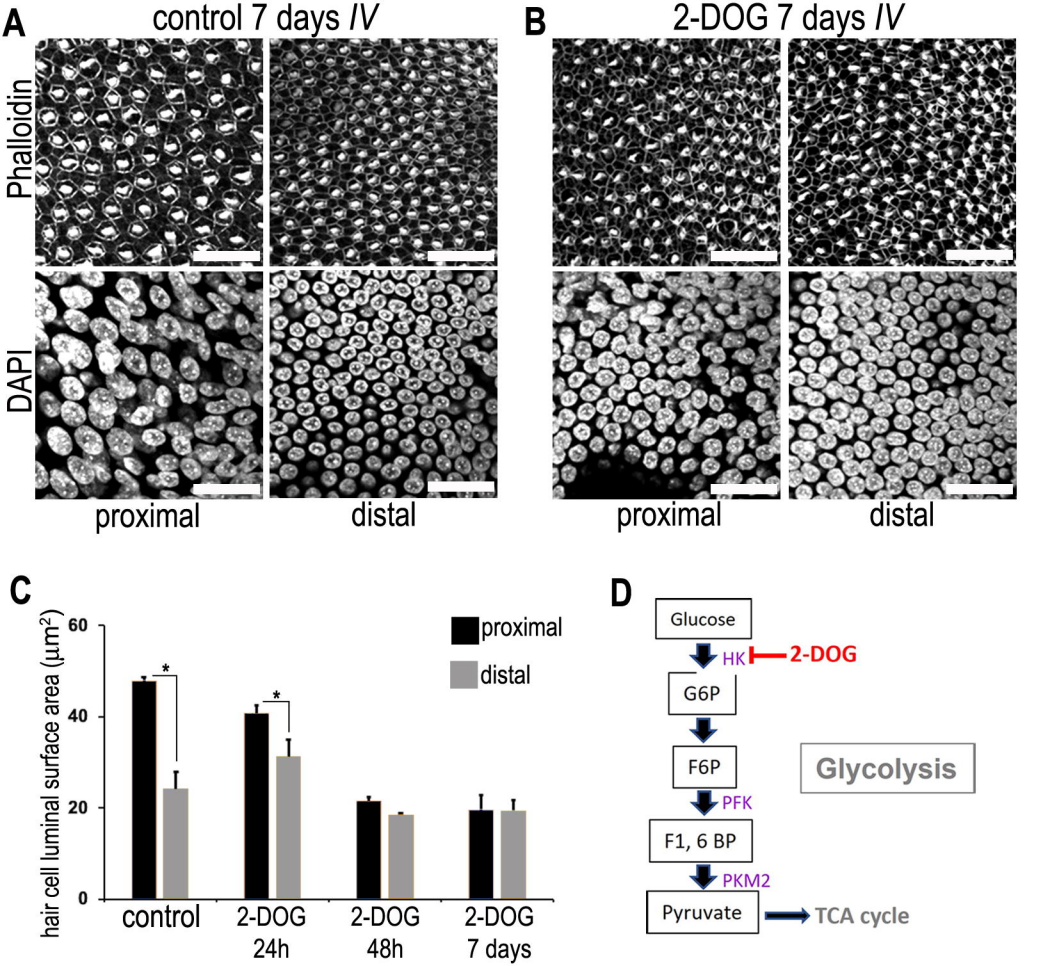
A
control 7 days IV
B
2-DOG 7 days IV
Phalloidin
DAPI
proximal
distal
proximal
distal
C
hair cell luminal surface area (μm²)
60
40
20
0
proximal
distal
*
*
control
2-DOG 24h
2-DOG 48h
2-DOG 7 days
D
Glucose
HK
2-DOG
G6P
F6P
Glycolysis
PFK
F1, 6 BP
PKM2
Pyruvate
TCA cycle

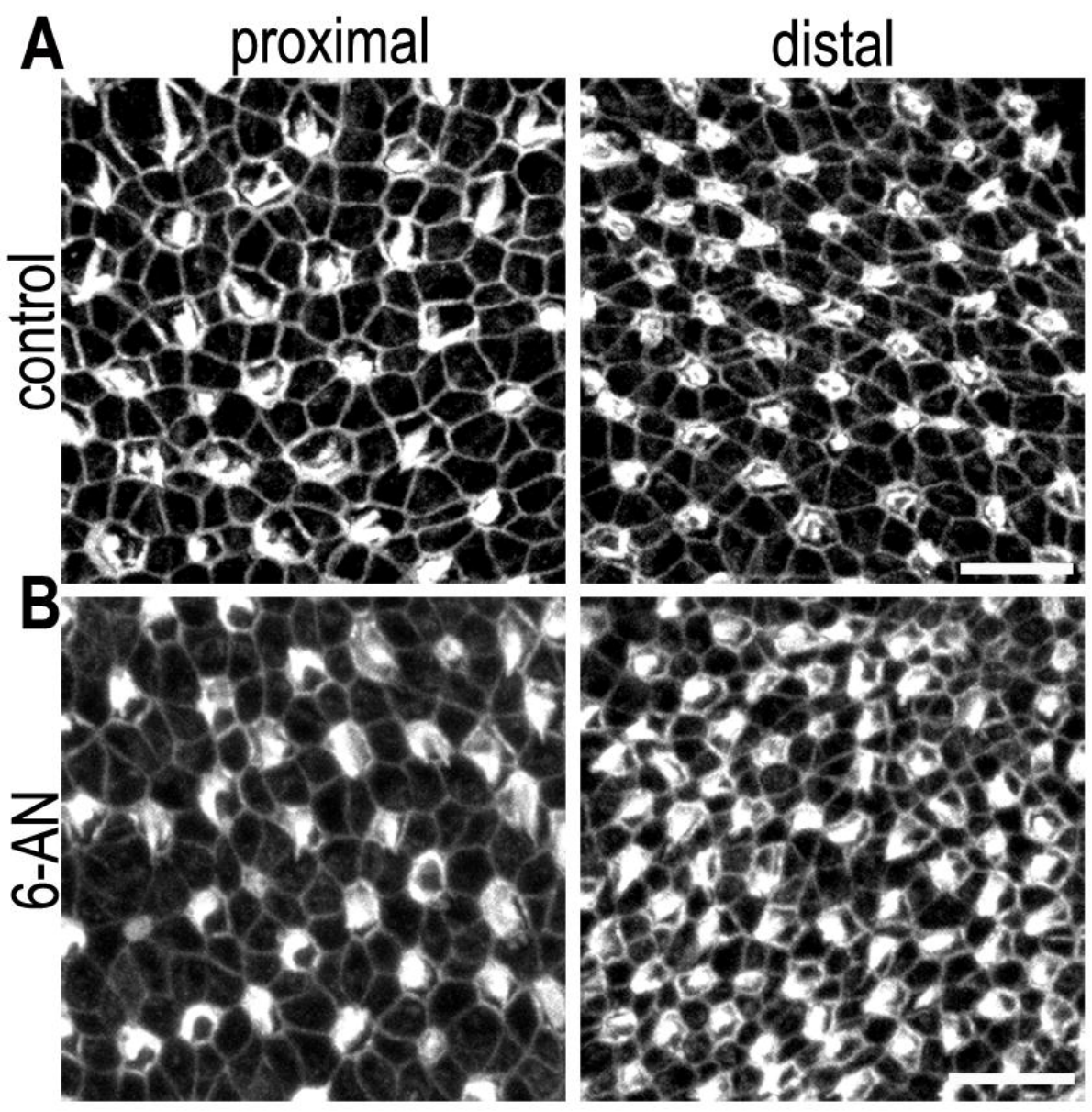
A
proximal
distal
control
B
6-AN

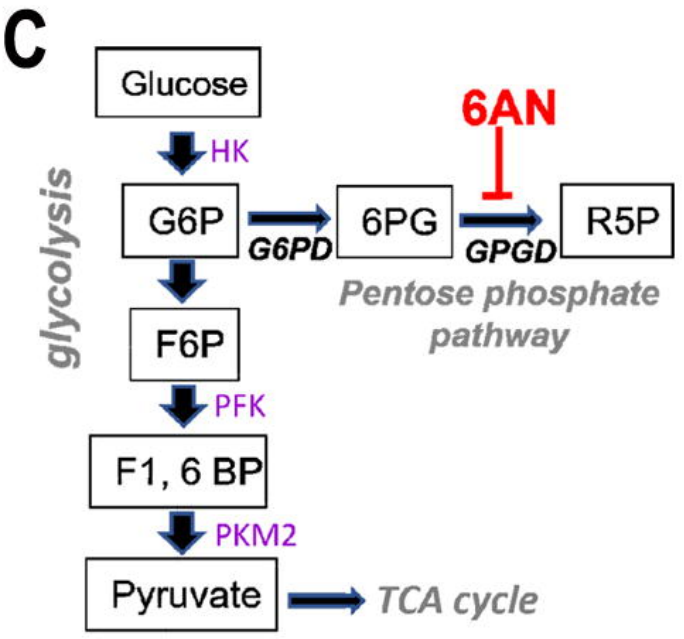
C
Glucose
HK
G6P
G6PD
6PG
6AN
GPGD
R5P
glycolysis
Pentose phosphate pathway
F6P
PFK
F1, 6 BP
PKM2
Pyruvate
TCA cycle

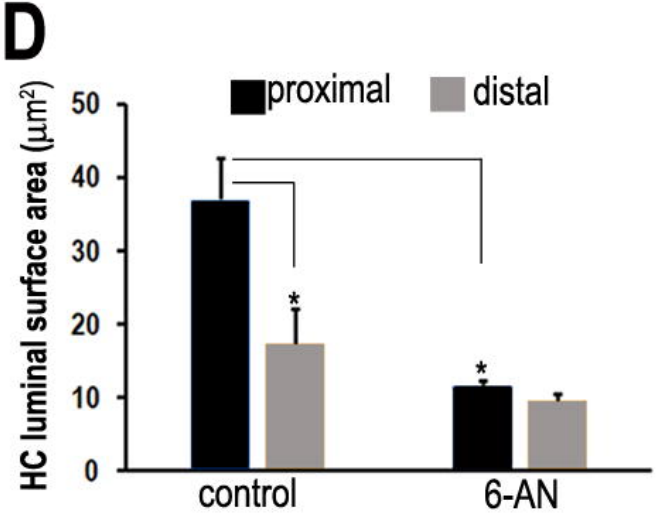
D
proximal
distal
HC luminal surface area (μm²)
50
40
30
20
10
0
control
6-AN

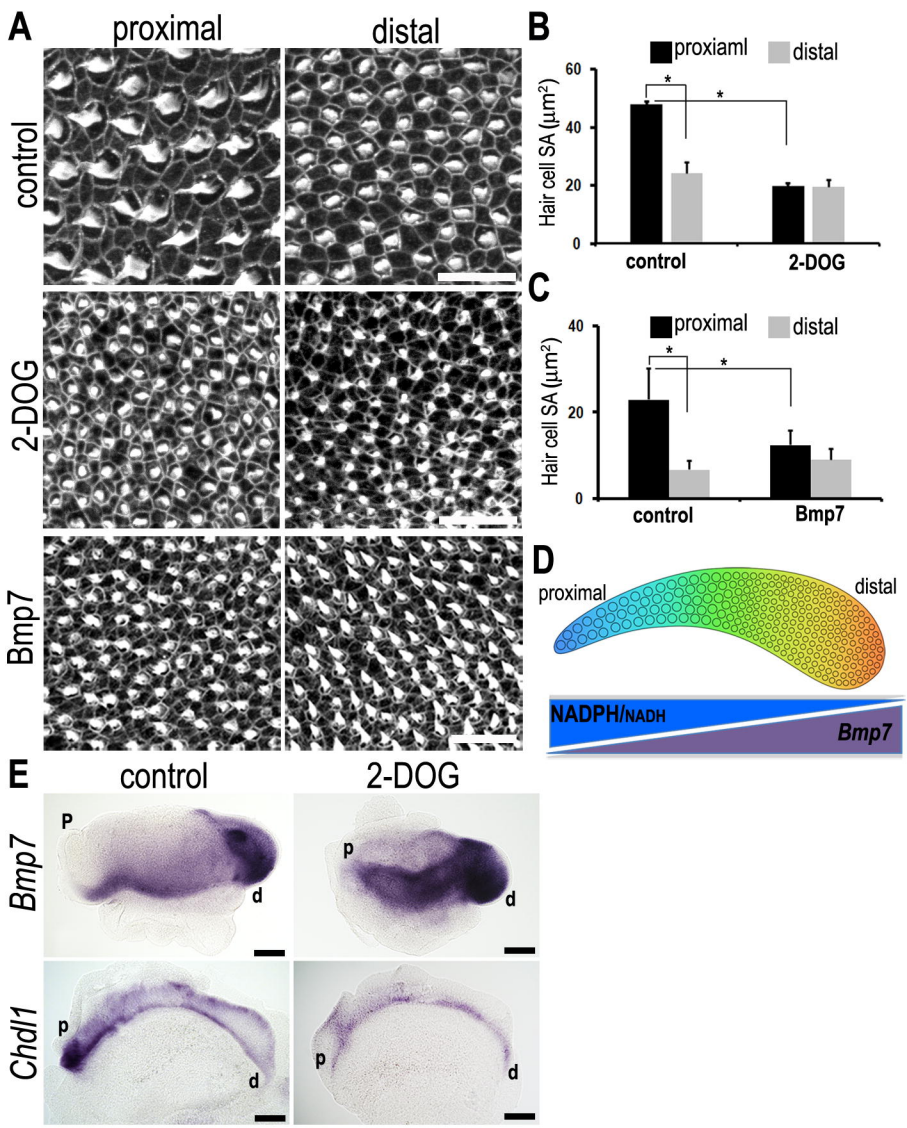
A
proximal
distal
control
2-DOG
Bmp7
B
proxiaml
distal
Hair cell SA (μm²)
60
40
20
0
*
*
control
2-DOG
C
proximal
distal
Hair cell SA (μm²)
40
20
0
*
*
control
Bmp7
D
proximal
distal
NADPH/NADH
Bmp7
E
control
2-DOG
Bmp7
Chdl1
p
d